INSTITUTE OF PHYSICS PUBLISHING JOURNAL OF PHYSICS B: ATOMIC, MOLECULAR AND OPTICAL PHYSICS

J. Phys. B: At. Mol. Opt. Phys. **39** (2006) R379–R424 doi:10.1088/0953-4075/39/22/R01

PhD TUTORIAL

A complete numerical approach to electron–hydrogen collisions

Philip L Bartlett

The ARC Centre for Antimatter–Matter Studies, Murdoch University, Perth 6150, Australia

E-mail: p.bartlett@murdoch.edu.au

Received 28 July 2006, in final form 14 September 2006
Published 27 October 2006
Online at stacks.iop.org/JPhysB/39/R379

Abstract

This tutorial presents an extensive computational study of electron-impact scattering and ionization of atomic hydrogen and hydrogenic ions, through the solution of the non-relativistic Schrödinger equation in coordinate space using propagating exterior complex scaling (PECS). It details the complete numerical and computational development of the PECS method, which enables highly computationally-efficient solution of these collision systems. Benchmark results are presented for a complete range of electron–hydrogen collisions, including discrete elastic and inelastic scattering both below and above the ionization threshold energy, very low-energy ionizing collisions through to moderately high-energy ionizing collisions, ground-state and excited-state targets and charged hydrogenic targets with $Z \leqslant 4$. Total ionization cross sections through to fully differential cross sections, both in-plane and out-of-plane, are given and are found to be in excellent accord with other state-of-the-art methods and measurements, where available. We also review our recent confirmation (Bartlett and Stelbovics 2004 *Phys. Rev. Lett.* **93** 233201) of the Wannier and related threshold laws for e–H collisions.

(Some figures in this article are in colour only in the electronic version)

Contents

1. Introduction

The collisions of electrons with atoms are fundamental to many physical processes, from the phosphorescent glow of computer screens and fluorescent lighting to the high temperature plasmas of the Sun, stars and tokamaks used for nuclear fusion power generation. The development of quantum theory in the early 1900s provided a theoretical basis for solving atomic collisions. Unfortunately, the Schrödinger equation that is fundamental to these collisions, only possesses analytic solutions for two-body systems. One of the simplest of atomic collisions, an electron impacting with a hydrogen atom (e–H), which is the subject of the PhD research summarized in this tutorial, has no known analytic solution. It is a testament to the complexity of collision problems that proceeding from two-body collisions to a three-body system has taken almost a further century to formulate and solve numerically.

There are three possible outcomes for e–H non-relativistic collisions: elastic scattering of the incident electron, inelastic scattering where the target is left in an excited state (that subsequently decays) and a break-up collision where the target is ionized, resulting in two free electrons. The excitation and ionization channels may be closed or open depending on whether the incident electron exceeds the required excitation and ionization threshold energies, respectively. Though a 'simple' collision system, the measured cross sections (interaction probabilities) for each of these channels have many structural features that vary with impact energy and the angular and energy distribution of the final-state electrons. The richness of these structures, along with the large body of available experimental data, makes this collision system an ideal test bed for new computational methods.

For nearly a century, atomic physicists have used approximation techniques in an effort to find analytic and numerical solutions to the e–H collision. Many of the modern numerical techniques have evolved from the close-coupling (CC) expansion introduced by Massey and Mohr [1], which expands the wavefunction for electron–atom collisions in terms of eigenstates of the target atom. However, the very limited computational resources available in this era meant that other more restrictive, but numerically tractable, approaches were developed including perturbation methods such as the Born approximation (e.g., see Massey and Mohr [2], Mott and Massey [3] and Omidvar [4]).

With the increasing availability of computing resources in the second half of last century, attention returned to the CC expansion technique. Burke and Taylor [5] were successful in describing the elastic and inelastic non-break-up collisions below the ionization threshold by introducing extra basis states in their CC expansion. When applied at higher energies, their results exhibited non-physical pseudo-resonance structures, which was simply an artefact of a still limited basis set. A larger pseudostate basis led to a better description of the effect of the continuum ionization channel, and resolved this problem [6]. Using a model problem, Bray and Stelbovics [7, 8] demonstrated that with a sufficiently large basis of eigenstates and positive-energy pseudostates convergent total cross sections could be obtained for all discrete and ionization processes at all energies, without unphysical resonance structures. Both this method, convergent close-coupling (CCC) [9, 10], and the intermediate energy *R*-matrix (IERM) method of Burke, Scott, Sholtz and coworkers [11–13] were then able to accurately calculate integrated scattering cross sections (ICS) for e–H collisions over a wide range of energies.

The ionization channel has proven the most difficult to solve for e–H collisions; the electrostatic forces have a long-ranged interaction and perturbation methods could not account for ionization measurements at low and intermediate electron energies. Bray and Stelbovics [14] showed that the positive-energy pseudostates included in their CCC calculations could be used to evaluate ionization cross sections, and obtained the first e–H total ionization cross section (TICS) results that were in complete agreement with experiment over a wide range of energies. In addition to CCC and IERM, other state-of-the-art methods include, for example, *R*-matrix with pseudostates (RMPS) [15], hyperspherical close-coupling (HSCC) [16] and time-dependent close-coupling (TDCC) [17]. All these methods are now in good agreement with e–H measurements for those kinematics, target-states and reaction channels to which they have been applied.

Given a sufficiently large basis, the pseudostate methods (IERM, RMPS and CCC) provide *ab initio* solutions. However, in practice they exhibit large unphysical oscillations in their ionization single-differential cross section (SDCS) results, with respect to (w.r.t.) energy sharing of the outgoing electrons, that are smoothed with various integral-preserving [18] and least-squares fitting [19] techniques. As discussed by Bray [20] and Stelbovics [21], it appears to be a feature of the CC expansions that the energy-sharing SDCS that they predict are not symmetric about equal energy-sharing, but rather exhibit a step-function behaviour.

Direct solutions for the time-independent Schrödinger equation are relatively simple to implement and the rapid increase in supercomputing performance has made them attractive. Rescigno, Baertschy, McCurdy and coworkers [22–24] demonstrated that an exterior complex scaling (ECS) transformation [25, 26], similar to that used for atomic resonance calculations, could be applied successfully to ionization problems. They obtained the first direct solutions for the scattering wavefunctions for e–H ionizing collisions in coordinate space, without explicit knowledge of the outer boundary conditions of their grid. Ionization cross sections were then calculated from these scattering wavefunctions using a surface integral method [27, 28] that includes an approximation of the final-state asymptotic continuum waves. The ability

of ECS to calculate differential ionization cross sections without application of empirical smoothing techniques is of significant benefit. As ECS evolves to targets with multiple active electrons, where the *a priori* assumption that the SDCS is smooth may not be valid, this feature will be a distinct advantage.

The impressive results and significant potential of the ECS method gave the impetus for the PhD project described in this tutorial. The goal of this investigation was threefold. Firstly, to generalize the ECS method and solve the non-relativistic time-independent Schrödinger equation for a *complete*[1] range of e–H collisions. Secondly, to develop numerical and computational algorithms that reduce the computational requirements of the ECS method for e–H collisions. Lastly, to undertake a thorough investigation of e–H ionizing collisions near the ionization threshold. Collisions at these energies have been problematic for all state-of-the-art methods. To maintain accuracy as energy approaches threshold, the direct methods require increasingly larger grids, while CC methods require an increasingly larger pseudostate basis, and computational resource limits are quickly reached. Using our enhanced numerical methods we sought to obtain the first fully-quantal *ab initio* support for the classically derived Wannier [29] and related threshold laws.

The results of the present work were obtained from a numerical grid in coordinate space using both exterior complex scaling and an enhancement of a propagation algorithm [30, 31] previously used for model e–H calculations. So as to differentiate this method from the ECS method [24], we will refer to the present work as the *propagating exterior complex scaling* method, and use the acronym PECS.

In section 2 we will develop the theoretical foundation of the PECS method by extending ECS to include excited initial-state and charged hydrogenic targets, and methods for calculating discrete final-state cross sections. Section 3 gives the numerical and computational development of PECS, including the propagation method, finite-difference scheme and iterative algorithms that greatly reduce computational effort. Section 4 gives a full analysis of the convergence of the PECS calculations with respect to all approximations. Section 5 applies PECS to a *complete* range of e–H collisions, followed by a summary in section 6 of our comprehensive investigation into near-threshold e–H ionizing collisions.

In addition to the PhD thesis [32], many publications [33–43] have emanated from the research described in this tutorial. However, the theoretical development here is the first to give the final form of the PECS equations for arbitrary initial states, and gives results for many targets and kinematics not included in these publications. This tutorial gives a comprehensive overview of the methods and results of the project, and the reader is directed to these previous works for further results and detailed descriptions.

2. Theoretical development

The ECS method is simple in its derivation as it solves the non-relativistic time-independent Schrödinger equation for the collision in a finite region of coordinate space, directly, completely and without knowledge of the boundary conditions, and as such is a fully *ab initio* method. Also, it does not rely on any specialized expansion techniques, using only an expansion in terms of angular momentum, which is used in a vast range of quantum-mechanical problems, and has a solid theoretical foundation. The high accuracy attainable with ECS is due to the

[1] In this context, *complete* should be taken to mean all reaction channels (elastic scattering, inelastic discrete final-state scattering and ionization), for targets in the ground state and excited states, both neutral hydrogen atoms and charged hydrogenic ions, and energies that are accessible to experimental measurement, ranging from below ionization threshold to moderately-high energies (within the constraints of the non-relativistic Schrödinger equation) where perturbation methods become accurate.

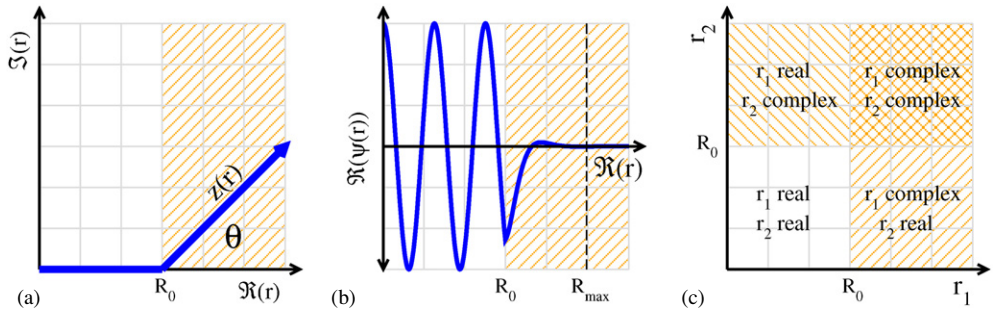

Figure 1. (a) Graphical representation of the rotation by θ rad into the complex plane of the radial coordinate $z(r)$ at the start of the complex scaling region R_0. (b) Result of exterior complex scaling of $\psi(r) = \sin(z(r))$. (c) Regions of complex scaling in a two-dimensional coordinate system.

minimal number of approximations used in its derivation and numerical solution, all of which can be considered as controlled as their errors are readily estimated from convergence studies.

The conventions used throughout this tutorial, unless stated otherwise, are that all quantities and equations are in atomic units (au), where $\hbar$, the electron mass m_e and the proton charge Z_p are set to unity; vectors and functions dependent upon vectors are given in bold font, e.g. $\mathbf{\Psi}(\boldsymbol{r}_1, \boldsymbol{r}_2)$, while scalars and functions dependent only upon scalar quantities are given an italic font, e.g. $\psi(r_1, r_2)$.

2.1. Exterior complex scaling

The use of an ECS transformation to obviate the requirement for asymptotic boundary conditions when solving atomic and molecular collisions was first described by Nicolaides and Beck [25], and independently suggested by Simon [26]. Many decades prior to this the complex rotation of the radial coordinates had been used for atomic resonance problems. However, it was not until 1997 that Rescigno *et al* [44] began exploring the use of ECS for three-body ionizing collisions, which culminated in their landmark publication in Science [22] of the first complete solution to an e–H break-up problem. These publications, along with [24, 45], should be referenced for a detailed description and theoretical justification of the ECS transformation; here we will use a simple one-dimensional example to give some insight into the workings of ECS.

The ECS transformation rotates the radial coordinates into the complex plane by a fixed angle $0 < \theta < \pi/2$ at a finite distance from the origin (R_0) using the transformation

$$z(r) \mapsto \begin{cases} r, & r < R_0 \\ R_0 + (r - R_0)\,\mathrm{e}^{\mathrm{i}\theta}, & r \geqslant R_0. \end{cases} \tag{1}$$

This is depicted graphically in figure 1(a). If we apply this transformation to a one-dimensional outgoing wave $\psi(r) = \mathrm{e}^{+\mathrm{i}r}$, for $r > R_0$ we obtain

$$\psi(r) \mapsto \psi(z(r)) = \exp(-(r - R_0)\sin\theta)\exp(\mathrm{i}(R_0 + (r - R_0)\cos\theta)) \xrightarrow[r\to\infty]{} 0, \tag{2}$$

which demonstrates that outgoing waves diminish exponentially beyond R_0 under this transformation. Figure 1(b) shows the real part of this wavefunction (with arbitrary units), where it is evident that the wavefunction diminishes by 99.9% within 1.5 oscillations from R_0. When solving differential equations numerically with the ECS method, we use this point ($R_{\max}$) as the edge of our grid and set the boundary condition at this point to zero with minimal

loss of accuracy. A discontinuity in the first derivative of the transformed wavefunction is observed at R_0, which affects the grid spacing required in this region. Rescigno *et al* [44] showed that the ECS transformation is valid for use with finite-difference methods, provided that the point of rotation into the complex plane R_0 is one of the points on the numerical grid.

If we now consider a one-dimensional incoming wave $\psi(r) = \mathrm{e}^{-ir}$, for $r > R_0$ we obtain

$$\psi(r) \mapsto \psi(z(r)) = \exp((r - R_0)\sin\theta)\exp(-\mathrm{i}(R_0 + (r - R_0)\cos\theta)) \xrightarrow[r\to\infty]{} \infty, \tag{3}$$

which demonstrates that incoming waves *diverge* under this transformation. It is important, therefore, to ensure that equations solved using ECS *do* have outgoing waves beyond R_0 and *don't* have incoming waves beyond R_0.

The ECS transformation is applied separately to both radial coordinates of the e–H equations, and figure 1(c) demonstrates the four regions where r_1 and r_2 are either real or complex. The solutions obtained using ECS are meaningful only in the region where both coordinates are real, $r_1, r_2 \leqslant R_0$.

2.2. Schrödinger equation

The theoretical development for the collisions considered in this tutorial begins with the time-independent Schrödinger equation for an e–H collision

$$(\hat{\boldsymbol{H}} - E)\boldsymbol{\Psi}_i^{S(+)} = 0, \tag{4}$$

where $\hat{\boldsymbol{H}}$ is the Hamiltonian operator, E is the total energy of the system and $\boldsymbol{\Psi}_i^{S(+)}$ is the outgoing wavefunction. The initial state of the system is given by the subscript i, which represents the momentum of the incident electron $\boldsymbol{k}_i$ and the initial state $|n_i l_i m_i\rangle$ and nuclear charge Z of the hydrogenic target. The spin angular momentum S of the system is an observable quantum state that is conserved in the collision, and each spin state may be solved separately. Using ECS to solve this equation in the present form, where all boundary conditions are zero, will give the trivial solution $\boldsymbol{\Psi}_i^{S(+)} = \boldsymbol{0}$. To resolve this problem we rearrange the equation into an inhomogeneous form by separating the outgoing wavefunction into an incident wave $\boldsymbol{\Psi}_{i,\mathrm{inc}}^{S}$ and an outgoing scattering wave $\boldsymbol{\Psi}_{i,\mathrm{sc}}^{S(+)}$, related by

$$\boldsymbol{\Psi}_i^{S(+)} = \boldsymbol{\Psi}_{i,\mathrm{inc}}^{S} + \boldsymbol{\Psi}_{i,\mathrm{sc}}^{S(+)}\ . \tag{5}$$

The Schrödinger equation for the collision becomes

$$(E - \hat{\boldsymbol{H}})\boldsymbol{\Psi}_{i,\mathrm{sc}}^{S(+)} = (\hat{\boldsymbol{H}} - E)\boldsymbol{\Psi}_{i,\mathrm{inc}}^{S}, \tag{6}$$

where the right-hand side (RHS) is known analytically, and hence provides an inhomogeneous equation that is suitable for solution using ECS.

For the collision systems considered in this tutorial, the nucleus of the target is sufficiently massive, relative to the incident electron, that it may be considered fixed in space and its kinetic energy operator ignored without affecting the accuracy of the calculations. The resulting Hamiltonian $\hat{\boldsymbol{H}}$ of the interaction comprises one- and two-electron operators and is given by

$$\hat{\boldsymbol{H}} = -\frac{1}{2}\boldsymbol{\nabla}_1^2 - \frac{1}{2}\boldsymbol{\nabla}_2^2 - \frac{Z}{r_1} - \frac{Z}{r_2} + \frac{1}{|\boldsymbol{r}_1 - \boldsymbol{r}_2|}, \tag{7}$$

where $Z \geqslant 1$.

Equation (6) requires solution in six dimensions, two radial and four angular, which makes the numerical solution in the present form computationally intractable. Instead, we use a partial-wave expansion

$$\boldsymbol{\Psi}_{i,\mathrm{sc}}^{S(+)}(\boldsymbol{r}_1, \boldsymbol{r}_2) = \frac{1}{r_1 r_2}\sum_{l_1 l_2 L M} \psi_{i,l_1 l_2}^{LMS\Pi}(r_1, r_2)\mathcal{Y}_{l_1 l_2}^{LM}(\hat{\boldsymbol{r}}_1, \hat{\boldsymbol{r}}_2) \tag{8}$$

to reduce the system to an infinite set of coupled radial equations, each having only two dimensions, where numerical convergence is obtained in practice with a small number of partial waves. $\mathcal{Y}_{l_1 l_2}^{LM}$ is a bipolar spherical harmonic function, which is nonzero only when

$$|l_1 - l_2| \leqslant L \leqslant |l_1 + l_2|, \tag{9}$$

where L is the partial-wave angular momentum, M is the projection of L onto the z-axis and l_1 and l_2 are the angular momenta of each electron (see [46, 47] for a detailed description of these functions and their properties). This effectively separates the radial and angular components of the scattering wavefunction, and is a common strategy for solving quantum-mechanical equations. We have introduced the label Π to specify the parity of the angular-momentum state, which is conserved in the collision, and is given by

$$(-1)^{\Pi} = (-1)^{L+l_1+l_2}, \tag{10}$$

where we have defined even (natural) parity as $\Pi = 0$ and odd parity as $\Pi = 1$.

An analytic form of the incident wavefunction is given by an incoming Coulomb wave $\boldsymbol{\Phi}_{\mathrm{c}}^{(-)}(Z-1; \boldsymbol{k}_i, \boldsymbol{r})$, which represents the electron moving in a field of central charge $Z-1$, multiplied by the wavefunction of the hydrogenic target $\boldsymbol{\Phi}_i(\boldsymbol{r})$. Here, the i subscript represents the charge Z and initial state $|n_i l_i m_i\rangle$ of the hydrogenic target. As the incident and bound electrons are indistinguishable, we symmetrize the incident wavefunction w.r.t. exchange of the electron coordinates $\boldsymbol{r}_1$ and $\boldsymbol{r}_2$. This gives the incident wavefunction the final form

$$\boldsymbol{\Psi}_{i,\mathrm{inc}}^{S}(\boldsymbol{r}_1, \boldsymbol{r}_2) = \tfrac{1}{\sqrt{2}}\big(\boldsymbol{\Phi}_i(\boldsymbol{r}_1)\boldsymbol{\Phi}_{\mathrm{c}}^{(-)}(Z-1; \boldsymbol{k}_i, \boldsymbol{r}_2) + (-1)^S \boldsymbol{\Phi}_i(\boldsymbol{r}_2)\boldsymbol{\Phi}_{\mathrm{c}}^{(-)}(Z-1; \boldsymbol{k}_i, \boldsymbol{r}_1)\big), \tag{11}$$

where to ensure that our derivation is equivalent to Baertschy *et al* [48] for $Z = 1$, the Coulomb wave is normalized so that

$$\boldsymbol{\Phi}_{\mathrm{c}}^{(-)}(0; \boldsymbol{k}, \boldsymbol{r}) = \mathrm{e}^{\mathrm{i}\boldsymbol{k}\cdot\boldsymbol{r}}. \tag{12}$$

To proceed, we use a partial-wave expansion for a Coulomb wave

$$\boldsymbol{\Phi}_{\mathrm{c}}^{(-)}(Z; \boldsymbol{k}, \boldsymbol{r}) = \frac{4\pi}{kr} \sum_{lm} \mathrm{i}^l \exp(-\mathrm{i}\sigma_l(Z,k))\phi_l(Z; k, r) Y_{lm}^*(\hat{\boldsymbol{k}}) Y_{lm}(\hat{\boldsymbol{r}}), \tag{13}$$

where $\phi_l(Z; k, r)$ is the regular Coulomb radial wavefunction normalized as $\phi_0(0; k, r) = \sin(kr)$, the Coulomb phase is given by

$$\sigma_l(Z,k) = \arg\left(\Gamma\left(l + 1 - \mathrm{i}\frac{Z}{k}\right)\right), \tag{14}$$

and Y_{lm} is the spherical harmonic function (see [46, 47]). We also separate the initial-state hydrogenic wavefunction into its radial and angular components

$$\boldsymbol{\Phi}_i(\boldsymbol{r}) = \frac{1}{r}\phi_{n_i l_i}(Z; r) Y_{l_i m_i}(\hat{\boldsymbol{r}}). \tag{15}$$

After substitution and simplification, the final form of the partial-wave expansion of the time-independent Schrödinger equation for an arbitrary partial wave $LMSl_1l_2$ becomes

$$\left(2E + \frac{\partial^2}{\partial r_1^2} + \frac{2Z}{r_1} - \frac{l_1(l_1+1)}{r_1^2} + \frac{\partial^2}{\partial r_2^2} + \frac{2Z}{r_2} - \frac{l_2(l_2+1)}{r_2^2}\right) \psi_{i,l_1 l_2}^{LMS\Pi}(r_1, r_2)$$
$$- 2\sum_{l_1' l_2'} \langle l_1 l_2 \| \frac{1}{r_{12}} \| l_1' l_2' \rangle_L \, \psi_{i,l_1' l_2'}^{LMS\Pi}(r_1, r_2) = \chi_{i,l_1 l_2}^{LMS\Pi}(r_1, r_2), \tag{16}$$

where

$$\chi_{i,l_1 l_2}^{LMS\Pi}(r_1, r_2) = \frac{2}{k_i} \sum_l \sqrt{2\pi(2l+1)} C_{l_i m_i l 0}^{LM} \mathrm{i}^l \exp(-\mathrm{i}\sigma_l(Z-1, k_i)) \times \Bigg\{ \Bigg(\langle l_1 l_2 \| \frac{1}{r_{12}} \| l_i l \rangle_L$$
$$- \frac{1}{r_2}\delta_{l_1 l_i}\delta_{l_2 l} \Bigg) \phi_{n_i l_i}(Z; r_1)\phi_l(Z-1; k_i, r_2) + (-1)^{S+\Pi}(1 \leftrightarrow 2) \Bigg\} \tag{17}$$

is the inhomogeneous term, $C^{LM}_{l_i m_i l 0}$ is a Clebsch–Gordan coefficient and $(1 \leftrightarrow 2)$ repeats the previous term in the braces but exchanges l_1 with l_2 and r_1 with r_2.

Equation (A.1) gives an analytic non-integral expression for $\langle l_1 l_2 \| \frac{1}{r_{12}} \| l_1' l_2' \rangle_L$, which is referred to as the reduced-matrix element of $\frac{1}{r_{12}}$. We should note that this matrix element does not connect states of different total angular momentum or parity, so the summation over $l_1' l_2'$ is limited to those that satisfy the parity relation $(-1)^{\Pi} = (-1)^{L+l_1'+l_2'}$ and $|l_1' - l_2'| \leqslant L \leqslant |l_1' + l_2'|$. The PhD thesis relating to this tutorial [32] gives a detailed description of the algebraic and quantum-mechanical steps used to obtain (16) along with all the necessary angular-momentum relations.

Equation (16) is valid for all bound states of the hydrogen and charged hydrogenic ion targets. For the special case of ground-state hydrogen targets we set $Z = 1$, $n_i = 1$, $l_i = 0$ and $m_i = 0$, which gives $M = 0$, $\Pi = 0$, $l = L$, $\sigma_l = 0$, $\phi_L(0; k_i, r) = \hat{j}_L(k_i r)$ and $C^{L0}_{00L0} = 1$, where $\hat{j}_L$ is the Riccati–Bessel function, and our derivation reduces to that given in [48].

2.3. Scattering amplitude

In this section we give equations for the scattering amplitude $\boldsymbol{F}^S_{ji}(\hat{\boldsymbol{k}}_j)$ for elastic and inelastic discrete final-state collisions determined from the scattering wavefunction $\Psi^{S(+)}_{i,\mathrm{sc}}(\boldsymbol{r}_1, \boldsymbol{r}_2)$.

Formally, the asymptotic behaviour of the time-independent outgoing scattering wavefunction for discrete final-state scattering, excluding the ionization channel, is defined in terms of the scattering amplitude as

$$\Psi^{S(+)}_{i,\mathrm{sc}}(\boldsymbol{r}_1, \boldsymbol{r}_2) \underset{\substack{r_2 \to \infty \\ r_1/r_2 \to 0}}{\sim} \frac{1}{\sqrt{2}} \sum_{n_j l_j m_j} \Phi^S_j(\boldsymbol{r}_1) \frac{\exp\left(\mathrm{i}(k_j r_2 + \frac{Z-1}{k_j} \ln(2k_j r_2))\right)}{r_2} \boldsymbol{F}^S_{ji}(\hat{\boldsymbol{k}}_j), \tag{18}$$

where we have arbitrarily chosen $\boldsymbol{r}_1$ for the bound electron and $\boldsymbol{r}_2$ for the scattered electron. The j subscript represents the final state $|n_j l_j m_j\rangle$ of the hydrogenic target with nuclear charge Z, and the initial state i is as defined previously (making $\boldsymbol{F}^S_{ji}(\hat{\boldsymbol{k}}_j)$ also dependent on $\boldsymbol{k}_i$, which is directed along the z-axis in our derivations). The leading constant $1/\sqrt{2}$ ensures that this wavefunction has the same normalization as our symmetrized scattering wavefunction, and through conservation of energy the magnitude of the initial and final momentum of the scattered electron are related by

$$k_j^2 = k_i^2 - Z^2 \left(\frac{1}{n_i^2} - \frac{1}{n_j^2} \right). \tag{19}$$

We calculate the scattering cross sections using the Peterkop [27] integral

$$\boldsymbol{I}^S_{ji}(\hat{\boldsymbol{k}}_j) \sim \int \mathrm{d}\boldsymbol{r}_1 \int \mathrm{d}\boldsymbol{r}_2 \; \Psi^{S(+)}_{i,\mathrm{sc}}(\boldsymbol{r}_1, \boldsymbol{r}_2)(\hat{\boldsymbol{H}} - E)\Phi^{S(-)*}_j(\boldsymbol{k}_j, \boldsymbol{r}_1, \boldsymbol{r}_2), \tag{20}$$

where $\Phi^{S(-)}_j$ is an incoming discrete final-state wavefunction whose form we specify later. This approach was suggested and developed by McCurdy *et al* [49] for model problems and as far as we are aware had not been applied to the full e–H problem.

In [32] we give the full theoretical development, which derives the relationship between the Peterkop integral and the scattering amplitude as

$$\boldsymbol{F}^S_{ji}(\hat{\boldsymbol{k}}_j) = -\frac{1}{2\pi} \boldsymbol{I}^S_{ji}(\hat{\boldsymbol{k}}_j). \tag{21}$$

Whereas, the ECS method calculates essentially exact e–H scattering wavefunctions, this method for obtaining scattering amplitudes relies on applying an asymptotic integral at a finite

radius. However, this is a *controlled* approximation and from a single scattering wavefunction we can easily investigate the radial convergence of (20) and estimate the error introduced by applying this asymptotic integral at finite radii.

A partial-wave expansion of (21) is obtained by substituting the partial-wave expansions for the scattering wavefunction (8) and Coulomb wavefunction (13), the asymptotic discrete final-state wavefunction

$$\boldsymbol{\Phi}_j^{S(-)}(\boldsymbol{k}_j, \boldsymbol{r}_1, \boldsymbol{r}_2) \underset{r_2\to\infty}{\sim} \tfrac{1}{\sqrt{2}}\left\{\boldsymbol{\Phi}_j(\boldsymbol{r}_1)\boldsymbol{\Phi}_{\mathrm{c}}^{(-)}(Z-1;\boldsymbol{k}_j,\boldsymbol{r}_2) + (-1)^S\boldsymbol{\Phi}_j(\boldsymbol{r}_2)\boldsymbol{\Phi}_{\mathrm{c}}^{(-)}(Z-1;\boldsymbol{k}_j,\boldsymbol{r}_1)\right\} \tag{22}$$

and the hydrogenic wavefunction (15). Note the second term in (22) is asymptotically zero. After applying the divergence theorem (which converts the volume integral to a surface integral) and simplifying, we obtain our final form for the scattering amplitude

$$\boldsymbol{F}_{ji}^S(\hat{\boldsymbol{k}}_j) = \sum_{l_2LM\Pi} \mathrm{i}^{-l_2}\exp(\mathrm{i}\sigma_{l_2}(Z-1,k_j))C^{LM}_{l_jm_jl_2M-m_j}Y_{l_2M-m_j}(\hat{\boldsymbol{k}}_j)f_{ji,l_2}^{LMS\Pi}, \tag{23}$$

where the summation is over all l_2LM such that $|l_j - l_2| \leqslant L \leqslant l_j + l_2, |M| \leqslant L$, which coherently sums all possible parity states, and where

$$\begin{aligned} f_{ji,l_2}^{LMS\Pi} \underset{r_2\to\infty}{\sim} -\frac{\sqrt{2}}{k_j}\int \mathrm{d}r_1\, r_2\phi_{n_jl_j}(Z;r_1)\Big\{&\phi_{l_2}(Z-1;k_j,r_2)\frac{\partial}{\partial r_2}\frac{1}{r_2}\psi_{i,l_jl_2}^{LMS\Pi}(r_1,r_2) \\ &- \psi_{i,l_jl_2}^{LMS\Pi}(r_1,r_2)\frac{\partial}{\partial r_2}\frac{1}{r_2}\phi_{l_2}(Z-1;k_j,r_2)\Big\}, \end{aligned} \tag{24}$$

is the partial-wave scattering amplitude. The ICS for a given S is then evaluated using

$$\sigma_{ji}^S = \frac{k_j}{k_i}\sum_{l_2LM\Pi}\left|f_{ji,l_2}^{LMS\Pi}\right|^2. \tag{25}$$

We have included an explicit summation over parity in (23) and (25) to emphasize the contribution of both parity states, but as parity is determined by $(-1)^\Pi = (-1)^{l_i+l_2+L}$ its inclusion is redundant. The total ICS is the sum of the cross sections for each spin state multiplied by the spin weighting factor $(2S+1)/4$,

$$\sigma_{ji} = \sum_S \frac{2S+1}{4}\,\sigma_{ji}^S, \tag{26}$$

and the spin-weighted differential scattering cross section (DCS) is given by

$$\frac{\mathrm{d}\sigma_{ji}}{\mathrm{d}\hat{\boldsymbol{k}}_j} = \frac{k_j}{k_i}\sum_S\frac{2S+1}{4}\left|\boldsymbol{F}_{ji}^S(\hat{\boldsymbol{k}}_j)\right|^2. \tag{27}$$

Other quantities related to the scattering cross section, and often the subject of experimental measurement, are the spin asymmetry, which gives the relative magnitude of the singlet and triplet cross sections, and the reduced Stokes parameters which contain information on the phase of the magnetic sub-level amplitudes. Spin asymmetry is defined in terms of the separate spin cross sections (without spin weighting) as

$$A_{ji} = \frac{\sigma_{ji}^0 - \sigma_{ji}^1}{\sigma_{ji}^0 + 3\sigma_{ji}^1}, \tag{28}$$

and is a dimensionless quantity in the range $-\frac{1}{3} \leqslant A_{ji} \leqslant 1$. The reduced Stokes parameters are calculated using the relations

$$\bar{P}_1 = 2\lambda - 1 \tag{29a}$$

$$\bar{P}_2 = -2\sqrt{2}R \tag{29b}$$

$$\bar{P}_3 = 2\sqrt{2}I, \tag{29c}$$

where the electron–photon correlation parameters are defined as

$$\lambda = \langle |f_0^2| \rangle / \sigma \tag{30a}$$

$$R = \Re\langle f_1 f_0^* \rangle / \sigma \tag{30b}$$

$$I = \Im\langle f_1 f_0^* \rangle / \sigma, \tag{30c}$$

and where σ is the 1s–np DCS summed over all magnetic sub-levels, the angle brackets represent the spin-averaged sum over singlet and triplet spin states and the normalized scattering amplitude is given by

$$f_{m_j} = \sqrt{k_j / k_i}\, \boldsymbol{F}^S_{ji}. \tag{31}$$

Several related parameters are the linear polarization parameter (P_l), charge cloud alignment angle (γ) and excitation coherence parameter (P^+), which are given by

$$P_l = \sqrt{\bar{P}_1^2 + \bar{P}_2^2} \tag{32a}$$

$$\gamma = \arg(\bar{P}_1 + \mathrm{i}\bar{P}_2)/2 \tag{32b}$$

$$P^+ = \sqrt{\bar{P}_1^2 + \bar{P}_2^2 + \bar{P}_3^2}. \tag{32c}$$

To improve their clarity, the dependence of these equations on the scattering angle is left as implied.

2.4. Ionization amplitude

In the initial application of ECS to e–H ionizing collisions, Rescigno *et al* [22] calculated ionization cross sections from the outgoing flux of the scattering wavefunctions. The cross sections, however, were not radially converged and their numerical grid could not extend to the very large radii required for convergence ($\gg$100 au), so extrapolation techniques were used. This proved to be inaccurate when the energy-sharing of the outgoing electrons was highly asymmetric, which at moderate collision energies is the region that has the highest contribution to the TICS. In later publications [23, 24, 28] they used the Peterkop [27] surface integral method, which overcame this problem and provided converged ionization cross sections. We will not repeat their derivations here, but simply give the relevant final equations, enhanced to include excited and charged hydrogenic targets.

The surface integral method extracts the ionization amplitude from the scattering wavefunction using an integral over the surface of a hypersphere of hyperradius $\rho = \sqrt{r_1^2 + r_2^2}$, excluding an overall phase factor (independent of ρ), and is given by

$$\boldsymbol{F}^S_i(\boldsymbol{k}_1, \boldsymbol{k}_2) = \sum_{l_1 l_2 L M \Pi} \mathrm{i}^{-l_1 - l_2} \exp(\mathrm{i}(\sigma_{l_1}(Z, k_1) + \sigma_{l_2}(Z, k_2)))\mathcal{Y}^{LM}_{l_1 l_2}(\hat{\boldsymbol{k}}_1, \hat{\boldsymbol{k}}_2) f^{LMS\Pi}_{i, l_1 l_2}(k_1, k_2), \tag{33}$$

where the partial-wave amplitude is given by

$$f^{LMS\Pi}_{i, l_1 l_2}(k_1, k_2) \underset{\rho\to\infty}{\sim} \frac{2}{\sqrt{\pi}} \frac{\rho}{k_1 k_2} \int_0^{\pi/2} \mathrm{d}\alpha \left\{ \phi_{l_1}(Z; k_1, r_1)\phi_{l_2}(Z; k_2, r_2) \frac{\partial}{\partial \rho} \psi^{LMS\Pi}_{i, l_1, l_2}(r_1, r_2) \right.$$
$$\left. - \psi^{LMS\Pi}_{i, l_1, l_2}(r_1, r_2) \frac{\partial}{\partial \rho} \phi_{l_1}(Z; k_1, r_1)\phi_{l_2}(Z; k_2, r_2) \right\}, \tag{34}$$

and where $\alpha = \arctan(r_2/r_1)$ is the hyperangle and $\boldsymbol{k}_1$ and $\boldsymbol{k}_2$ are the momenta of the continuum electrons after the collision. Once again, we have included an explicit summation over parity states in (33) to emphasize the coherent addition of parity states, though its inclusion is redundant.

In order for (33) to converge in phase, Peterkop suggested that the charges on the Coulomb waves should satisfy

$$\frac{Z_1}{k_1} + \frac{Z_2}{k_2} = \frac{1}{k_1} + \frac{1}{k_2} - \frac{1}{|\boldsymbol{k}_1 - \boldsymbol{k}_2|}, \tag{35}$$

which is known as the Peterkop condition. There is no known analytic form for this condition when the integral is expanded in partial waves, and cannot be applied to (34). For the ionization of ground-state hydrogen, Baertschy *et al* [23] found that provided the same ρ was used for all partial waves, the phase ambiguities introduced by using uniform charges ($Z_1 = Z_2 = 1$) cancelled and the ionization *cross sections* were radially convergent.

The Peterkop formulation and phase factor divergence problem have been recently addressed in a series of papers by Kadyrov *et al* [50, 51]. They showed by a general argument that the practical procedure of choosing $Z_1 = Z_2 = 1$ is optimal, though when applied at finite ρ the ionization amplitude will contain radially-diminishing oscillations in both phase and magnitude. These oscillations are observed in our calculations, though generally ρ is sufficiently large that their magnitude is not significant. Importantly, their work supports the validity of this method for extracting ionization cross sections, but does emphasize its inability to give correct and converged ionization amplitude phase information. Kadyrov *et al* [51] give corrections to the method used here that will give formally correct ionization amplitude phases, if required.

The total ionization cross section for a given S is evaluated from the ionization amplitude using

$$\sigma_i^S = \sum_{\substack{l_1 l_2 \\ LM\Pi}} \int_0^{E/2} \mathrm{d}\epsilon_2 \, \frac{k_1 k_2}{k_i} \left| f_{i,l_1 l_2}^{LMS\Pi}(k_1, k_2) \right|^2. \tag{36}$$

where ϵ_2 is the energy of one of the outgoing electrons. As the scattering wavefunction is symmetrized w.r.t. electron exchange, the energy integration is limited to $E/2$.

The total ionization cross section (with spin weighting) is given by

$$\sigma_i = \sum_S \frac{2S+1}{4} \, \sigma_i^S, \tag{37}$$

the fully-differential ionization cross section (with spin weighting) is given by

$$\frac{\mathrm{d}\sigma_i}{\mathrm{d}\hat{\boldsymbol{k}}_1 \, \mathrm{d}\hat{\boldsymbol{k}}_2 \, \mathrm{d}\epsilon_2}(\boldsymbol{k}_1, \boldsymbol{k}_2) = \sum_S \frac{2S+1}{4} \frac{k_1 k_2}{k_i} \left| \boldsymbol{F}_i^S(\boldsymbol{k}_1, \boldsymbol{k}_2) \right|^2, \tag{38}$$

and the spin asymmetry is as defined in (28), though with suitable adjustment of the subscripts so as to refer to the ionization cross sections.

3. Numerical methods

Equation (16) gives the partial-wave time-independent Schrödinger equation for e–H collisions with arbitrary initial state, and has no known analytic solution. However, it is a relatively simple, coupled, second-order differential equation that can be solved using numerical

approximation techniques if sufficient boundary conditions are known. Two known boundary conditions are

$$\psi^{LMS\Pi}_{i,l_1l_2}(r_1, 0) = 0 \qquad \text{and} \qquad \psi^{LMS\Pi}_{i,l_1l_2}(0, r_2) = 0, \tag{39}$$

and using exterior complex scaling (1) we can closely approximate the outer boundary conditions by

$$\psi^{LMS\Pi}_{i,l_1l_2}(r_1, R_{\max}) \approx 0 \qquad \text{and} \qquad \psi^{LMS\Pi}_{i,l_1l_2}(R_{\max}, r_2) \approx 0, \tag{40}$$

where $R_{\max}$ is made sufficiently larger than R_0 (the start of the complex scaling region) such that exponential damping allows the outer boundary condition to be set arbitrarily close to zero. We now have sufficient boundary conditions to solve (16) numerically.

Rescigno *et al* [22] demonstrated that radially convergent solutions are obtained for e–H collisions at low-intermediate energies by setting the grid size sufficiently large ($R_0 \approx$ 100 au), ensuring that the Coulomb interactions are effectively complete. To investigate energies approaching ionization threshold an increasingly larger R_0 is required for convergence, and at higher energies or for excited initial-states a greatly increased number of L partial waves and coupled states of angular momentum (l_1, l_2) must be included. In this section, we will develop an alternative numerical method for finding solutions to the ECS equations that has proven to be extremely computationally efficient. This PECS method allows very-low energy, moderately-high energy and excited initial-state collisions of hydrogen and hydrogenic ions to be explored easily with moderate computing resources.

3.1. Numerical grid

Selecting an appropriate grid is the first step towards minimizing the computational effort required to numerically solve e–H collisions. Though the ECS technique has been demonstrated with both finite element and finite-difference numerical methods [22, 44], we will restrict our discussion to numerical grids that support finite-difference methods suitable for use with the propagation technique introduced later.

If we consider the symmetry of the e–H scattering wavefunction w.r.t. exchange of the radial coordinates

$$\psi^{LMS\Pi}_{i,l_1l_2}(r_1, r_2) = (-1)^{S+L+l_1+l_2}\psi^{LMS\Pi}_{i,l_2l_1}(r_2, r_1), \tag{41}$$

then we have two choices for solving the wavefunctions that minimize duplicate computations. We can solve for (a) a square grid $r_1, r_2 \leqslant R_{\max}$ and only $l_1 \leqslant l_2$, as undertaken by Rescigno *et al* [22], or (b) a triangular grid $r_2 \leqslant r_1 \leqslant R_{\max}$ for all (l_1, l_2).

For the present, let us make the simplistic assumption that finding solutions to our coupled grid equations requires $O(N^x)$ mathematical operations, where N is the number of points in our coupled grids, $x > 1$, and that we only consider even parity. For $L = 0$, where $l_1 = l_2$, method (b) requires half of the grid points, resulting in a $O(2^x)$ reduction in computational effort. For odd L, where $l_1 \neq l_2$, both methods are equivalent, and for even L method (b) has a $O([4/3]^x)$ reduction for $L = 2$, but diminishes to unity for higher L.

Clearly, using a triangular grid gives computational advantages, especially for the $L = 0$ partial waves that are used in most model calculations. Triangular grids have previously been successful for *model* e–H scattering [30] and ionization [52] problems and for the full e–H *scattering* problem [53, 54].

The second consideration when attempting to minimize computational effort is to maximize grid spacing (reducing grid points) while maintaining the required numerical accuracy. Previous model calculations [55] showed that finer grid spacing is required near the

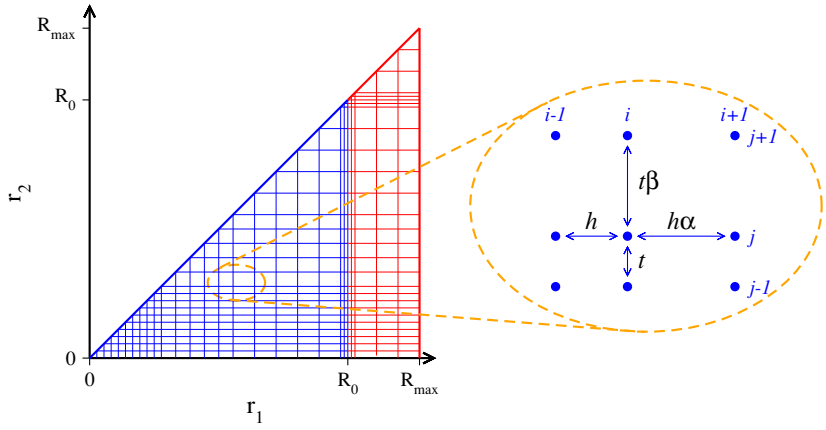

Figure 2. Triangular grid bounded by $r_2 = 0, r_1 = R_{\max}$ and $r_1 = r_2$. Real grid points are at intersecting blue lines ($r_1 \leqslant R_0$) and complex grid points are at intersecting red lines ($r_1 > R_0$). The inset shows the grid spacing h and t (real or complex), and the grid column and row numbers (i, j) in the r_1 and r_2 directions, respectively. The grid expansion (or contraction) ratios α and β may be real or complex, where $\alpha = \beta = 1$ would represent uniform grid spacing about (i, j).

nucleus (where Coulomb potentials are stronger) than for the outer region, which is consistent with ECS calculations [48].

A representative grid is shown in figure 2, which uses varying spacing in the real region and finer spacing about the transition to complex scaling (R_0) where the scattering wavefunction has discontinuous derivatives. Note that the grid spacing is symmetric w.r.t. exchange of r_1 and r_2, and that the finite-difference scheme must allow different spacing in each direction as well as a transition from real to complex spacing of one or both coordinates.

3.2. Numerov formulae

To simplify our discussion, we will initially consider a one-dimensional evenly spaced grid. These grids are suitable for simple finite-difference methods [56, p 884] that estimate second-order derivatives using $n \geqslant 3$ evenly spaced grid points (n is odd) and have an error $O\left(\{h^{n-1}\}\psi_i^{(n+1)}\right)$, where h is the grid spacing and $\psi_i^{(n+1)}$ is the $(n+1)$th derivative of ψ at the ith grid point. In fact, these formulae were used by Baertschy *et al* [48] for their ECS implementation, though adapted for variable grid spacing. We used a very accurate 3-point Numerov finite-difference formula that can evaluate second-order differential equations that have no first-derivative terms, as in (16). In one dimension, these equations have the form

$$\frac{\mathrm{d}^2}{\mathrm{d}r^2}\psi(r) + \Omega(r) = 0, \tag{42}$$

and the Numerov formula relates three successive points of ψ ($i-1$, i and $i+1$) along r by

$$\psi_{i+1} = 2\psi_i - \psi_{i-1} - \frac{h^2}{12}\left(\Omega_{i+1} + 10\Omega_i + \Omega_{i-1}\right), \tag{43}$$

and has a leading-order error of

$$\frac{h^6}{240}\psi_i^{(6)}. \tag{44}$$

This error is comparable to the standard 7-point finite-difference method, though the sparse-matrix linear equation built using the Numerov formulae has fewer nonzero diagonals, giving a significant computational advantage.

The Numerov formula has been used successfully for e–H model problems for scattering [30] and ionization [52] and the full e–H *scattering* problem [54], but to our knowledge has not previously been adapted for variable grids. Jones and Stelbovics [55] used a grid-doubling method that allowed their grid spacing to be increased by integer multiples (whilst continuing to use evenly spaced points for the Numerov formula). This technique is not suitable for the transition from real to complex coordinates at R_0 in our grid. Therefore, we derived a Numerov-like formula that allows for completely variable, and complex, changes in grid spacing.

Firstly, we proposed that a variable-spacing Numerov formula has the form

$$\psi_{i+1} = A\psi_i - B\psi_{i-1} - \frac{h^2}{12}\left(C\Omega_{i+1} + D\Omega_i + E\Omega_{i-1}\right), \tag{45}$$

where h is the grid spacing between r_{i-1} and r_i, and $h\alpha$ is the grid spacing between r_i and r_{i+1}. By substituting Taylor series expansions of ψ_{i-1} and ψ_{i+1}, about ψ_i, we solved the unknown coefficients, which gave

$$\begin{aligned}\psi_{i+1} = (\alpha+1)\psi_i - \alpha\psi_{i-1} - \frac{h^2}{12}\{&(\alpha^2+\alpha-1)\Omega_{i+1} + (\alpha^3+4\alpha^2+4\alpha+1)\Omega_i \\ &+ (-\alpha^3+\alpha^2+\alpha)\Omega_{i-1}\},\end{aligned} \tag{46}$$

and a leading-order error of

$$\left(\frac{\alpha^5}{180} + \frac{\alpha^4}{72} - \frac{\alpha^2}{72} - \frac{\alpha}{180}\right) h^5 \psi_i^{(5)}, \tag{47}$$

which is of the same order of magnitude as the variable-grid 7-point finite-difference formulae [48]. Equation (46) reduces to (43) for fixed grid spacing ($\alpha = 1$), and (47) reduces to zero. In this case the error is given by the next term in the series, which for $\alpha = 1$ reduces to (44).

This one-dimensional formula is readily extended to two dimensions using similar techniques to Poet [30]. There is, however, an additional complexity when reforming the scattering wave equation (16) into the form of (42); for $l = 0$ there is a $1/r$ singularity and for $l > 0$ there is also a $1/r^2$ singularity. We resolved this problem in the same way as Wang and Callaway [53], using the known limiting behaviour of the e–H scattering wavefunction

$$\psi_l(r) \to a r^{l+1} \qquad \text{as} \quad \mathrm{r} \to 0, \tag{48}$$

where a is a constant. Our modified Numerov formulae are presented in appendix B.

In figure 3, we see that one or more of the nine grid points required for the two-dimensional Numerov formula fall outside of the triangular grid when $i = j$ or $i = j + 1$. In this case, we use the symmetry of the scattering wavefunctions given in (41) to replace ψ_{ij} of partial wave $(l_1 l_2)$ with ψ_{ji} of partial wave $(l_2 l_1)$ multiplied by $(-1)^{S+L+l_1+l_2}$. This imposes two conditions on our numerical grids: the grid must be symmetric w.r.t. exchange of r_i and r_j, and both $(l_1 l_2)$ and $(l_2 l_1)$ must be included in the calculation (when $l_1 \neq l_2$).

3.3. Propagation method

Using the grid described in section 3.1 and the Numerov formulae in appendix B, it is now possible to construct and solve a single matrix equation for the e–H scattering wavefunctions for each $|LMS\Pi\rangle$. Though we expect computational savings for some partial waves from using a triangular grid, and additional savings with the Numerov formula, many limitations

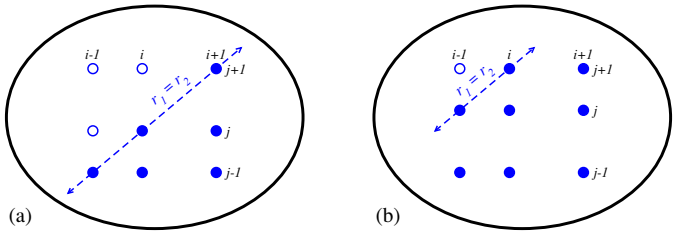

Figure 3. Grid points marked with hollow circles, needed for the two-dimensional Numerov formula, fall outside of the triangular grid ($r_j \leqslant r_i$, $r_j = 0$ and $r_i = R_{\max}$) when the central grid point is at (a) $i = j$, or (b) $i = j + 1$.

of this approach remain. The matrix equations are of such large magnitude that they are computationally intractable using sparse-matrix LU-factorization algorithms that require $O(N^2)$ mathematical operations.

Baertschy *et al* [48] found that a conjugate gradient squared (CGS) algorithm could iteratively solve their matrix equation with $O(N^{3/2})$ operations by using an approximate solution as a preconditioner. They also found that solutions to the uncoupled scattering wave equations (which require significantly less computational resources) could be used for these preconditioners. However, at total energies close to the ionization threshold, the strong electron correlation made these uncoupled solutions unsuitable for use as a preconditioner, and the CGS iterations did not converge.

In an attempt to further reduce the computational overhead of the e–H problem we used the propagation method, based on Poet [30], that was recently used by Jones and Stelbovics [31] for model e–H ionization problems. However, to allow for the inhomogeneous term χ in the scattering wave (16), this procedure required modification.

Rather than solving one large sparse-matrix equation (using complex arithmetic) for the whole grid, the propagation method 'solves' one column (or vector) of grid points $\vec{\psi}^{(i)}$ at a time by finding a propagating matrix $\boldsymbol{D}^{(i)}$ that relates it to the next column $\vec{\psi}^{(i+1)}$. This requires $i_{\max}$ small dense-matrix equations to be solved ($i_{\max}$ represents the grid column number associated with $R_{\max}$). As a starting point, we proposed that the propagation equation has the form

$$\vec{\psi}^{(i)} = \boldsymbol{D}^{(i)} \cdot \vec{\psi}^{(i+1)} + \vec{\boldsymbol{E}}^{(i)}, \tag{49}$$

where the propagation vector $\vec{\boldsymbol{E}}^{(i)}$ is introduced into our derivation to allow for the inhomogeneous term in (16).

The two-dimensional variable-grid Numerov formula (B.2) is then reformed into a matrix equation

$$\boldsymbol{A}^{(i)} \cdot \vec{\psi}^{(i-1)} + \boldsymbol{B}^{(i)} \cdot \vec{\psi}^{(i)} + \boldsymbol{C}^{(i)} \cdot \vec{\psi}^{(i+1)} = \vec{\boldsymbol{F}}^{(i)} \tag{50}$$

that relates the $i - 1$, i and $i + 1$ columns of the grid using the eight nearest neighbours for each point ψ_{ij} in the column. We should note that all coupled (l_1, l_2) angular momenta for the $LMS\Pi$ partial wave must be solved simultaneously, and if we let n_c represent the number of (l_1, l_2) pairs required for convergence of the partial wave, we must solve n_c triangular grids simultaneously. Therefore, each $\vec{\psi}^{(i)}$ vector will contain $n_c i$ grid points. The boundary points with $r_j = 0$ are not included in these vectors.

Substituting (49) into (50) gives

$$\boldsymbol{D}^{(i)} = -\tilde{\boldsymbol{B}}^{(i)} \cdot \boldsymbol{C}^{(i)} \tag{51}$$

Table 1. Characteristics of the matrices and vectors used in equations (49)–(53), where i is the grid column number and n_s is the number of simultaneously (not iteratively) coupled wavefunctions and n_d is the number of nonzero diagonals in the matrix. The storage requirement is a first-order estimate that assumes double-precision arithmetic (8 B per real floating-point number). The total storage may be calculated by summing over all i.

Matrix/ vector	Size (rows × columns)	Density	n_d	Variable type		Storage (B)	
				$i < i_{R_0}$	$i \geqslant i_{R_0}$	$i < i_{R_0}$	$i \geqslant i_{R_0}$
$\boldsymbol{A}^{(i)}$	$n_s i \times n_s(i-1)$	Banded	$3n_s$	Real	Complex	$24n_s^2 i$	$48n_s^2 i$
$\boldsymbol{B}^{(i)}$	$n_s i \times n_s i$	Banded	$3n_s$	Real	Complex	$24n_s^2 i$	$48n_s^2 i$
$\tilde{\boldsymbol{B}}^{(i)}$	$n_s i \times n_s i$	Dense	–	Real	Complex	$8n_s^2 i^2$	$16n_s^2 i^2$
$\boldsymbol{C}^{(i)}$	$n_s i \times n_s(i+1)$	Banded	$3n_s$	Real	Complex	$24n_s^2 i$	$48n_s^2 i$
$\boldsymbol{D}^{(i)}$	$n_s i \times n_s(i+1)$	Dense	–	Real	Complex	$8n_s^2 i^2$	$16n_s^2 i^2$
$\vec{\boldsymbol{E}}^{(i)}$	$n_s i \times 1$	–	–	Complex	Complex	$16n_s i$	$16n_s i$
$\vec{\boldsymbol{F}}^{(i)}$	$n_s i \times 1$	–	–	Complex	Complex	$16n_s i$	$16n_s i$
$\vec{\psi}^{(i)}$	$n_s i \times 1$	–	–	Complex	Complex	$16n_s i$	$16n_s i$

and

$$\vec{\boldsymbol{E}}^{(i)} = \tilde{\boldsymbol{B}}^{(i)} \cdot (\vec{\boldsymbol{F}}^{(i)} - \boldsymbol{A}^{(i)} \cdot \vec{\boldsymbol{E}}^{(i-1)}), \tag{52}$$

where

$$\tilde{\boldsymbol{B}}^{(i)} = (\boldsymbol{B}^{(i)} + \boldsymbol{A}^{(i)} \cdot \boldsymbol{D}^{(i-1)})^{-1}. \tag{53}$$

The size and density of each of these matrices are summarized in table 1, where it should be noted that the matrices are real for $i < i_{R_0}$, which offers a four-fold reduction in computational effort in comparison to 'all-complex' numerical approaches.

To begin the propagation at the first column ($i = 1$) we note that $\boldsymbol{A}^{(1)}$ is a null vector and $\boldsymbol{D}^{(0)}$ and $\vec{\boldsymbol{E}}^{(0)}$ are not required to be known, and in fact are also null. We can therefore reduce (51) and (52) to

$$\boldsymbol{D}^{(1)} = -(\boldsymbol{B}^{(1)})^{-1} \cdot \boldsymbol{C}^{(1)} \tag{54}$$

and

$$\vec{\boldsymbol{E}}^{(1)} = (\boldsymbol{B}^{(1)})^{-1} \cdot \vec{\boldsymbol{F}}^{(1)}, \tag{55}$$

respectively.

After solving $\boldsymbol{D}^{(1)}$ and $\vec{\boldsymbol{E}}^{(1)}$, the remaining $\boldsymbol{D}^{(i)}$ and $\vec{\boldsymbol{E}}^{(i)}$ are evaluated in ascending i order, followed by $\vec{\psi}^{(i)}$ in reverse order ($i = i_{\max} - 1$ to $i = 1$) using (49) and the ECS boundary condition $\vec{\psi}^{(i_{\max})} = \vec{\boldsymbol{0}}$. Hence, the PECS method solves the coupled scattering wave equation in $2(i_{\max} - 1)$ steps, where the vast majority of the computational effort is devoted to the $i_{\max} - 1$ matrix inversions in (53). It should be stressed that this method does *not* rely on an initial approximation for $\psi^{LMS\Pi}_{i,l_1 l_2}$, or iterative refinement, as in the ECS/CGS method, and will find solutions for collisions at total energies very close to ionization threshold.

3.4. Iterative-coupling method

The vast majority of the computations required by the PECS method are devoted to the matrix inversion in (53), which is *independent* of $\vec{\boldsymbol{F}}$ and hence the RHS of (16). In this section, we will show how this feature can be exploited to obtain a highly efficient iterative coupling scheme for the PECS method.

The iterative coupling scheme for PECS was inspired, in part, by the ECS/CGS method [48], which solves the sparse linear equations for e–H collisions using an uncoupled solution as a preconditioner followed by iterative refinement. This suggests that coupling for e–H collisions may be treated as a perturbation to the uncoupled equations, at least for energies greater than 1 eV above threshold. The Schrödinger equation for e–H collisions (16) and (17) can be rearranged into an iterative form, where the first iteration finds the uncoupled solution. Further iterations incorporate estimates for the coupled wavefunctions based upon the previous iteration, and the results converge towards the fully coupled solutions. To simplify the labelling of our iterative scheme, the labels a and b are used to represent the bth iteration of the ath coupled partial wave $\left|LMS\Pi l_1^a l_2^a\right\rangle$, where $1 \leqslant a \leqslant n_c$ and n_c is the number of separate (l_1, l_2) required to achieve convergence of the $LMS\Pi$ partial waves. The iterative equivalent of (16) becomes

$$\left(2E + \frac{\partial^2}{\partial r_1^2} + \frac{2Z}{r_1} - \frac{l_1^a\left(l_1^a+1\right)}{r_1^2} + \frac{\partial^2}{\partial r_2^2} + \frac{2Z}{r_2} - \frac{l_2^a\left(l_2^a+1\right)}{r_2^2} - 2\left\langle l_1^a l_2^a \middle\| \frac{1}{r_{12}} \middle\| l_1^a l_2^a \right\rangle_L\right) \times \overline{\psi}^{LMS\Pi}_{i,l_1^a l_2^a,b+1}(r_1, r_2) = \overline{\xi}^{LMS\Pi}_{i,l_1^a l_2^a,b+1}(r_1, r_2), \tag{56}$$

where $b \geqslant 0$, and

$$\overline{\xi}^{LMS\Pi}_{i,l_1^a l_2^a,b+1}(r_1, r_2) = \chi^{LMS\Pi}_{i,l_1^a l_2^a}(r_1, r_2) + 2\sum_{a' \neq a} \left\langle l_1^a l_2^a \middle\| \frac{1}{r_{12}} \middle\| l_1^{a'} l_2^{a'} \right\rangle_L \overline{\psi}^{LMS\Pi}_{i,l_1^{a'} l_2^{a'},b}(r_1, r_2), \tag{57}$$

where setting $\overline{\psi}^{LMS\Pi}_{i,l_1^{a'} l_2^{a'},0}(r_1, r_2) = 0$ ensures that no coupling of other partial waves occurs on the first iteration ($b = 0$). The net result of this rearrangement is that coupling of wavefunctions with different (l_1, l_2) is moved to the RHS. For subsequent iterations ($b > 0$) estimates for coupled wavefunctions ($a' \neq a$) are obtained from the previous iteration. The overbars in (56) and (57) are used to differentiate the iteratively-coupled approximation from a fully-coupled solution.

We can see from (50) and (B.1) that reforming the Schrödinger equation in this way affects the construction of the $\boldsymbol{A}^{(i)}$, $\boldsymbol{B}^{(i)}$ and $\boldsymbol{C}^{(i)}$ matrices, though they remain the same for each iteration, while $\overrightarrow{\boldsymbol{F}}^{(i)}$ changes with each iteration. Consequently, $\tilde{\boldsymbol{B}}^{(i)}$ (and its associated matrix inversion) are only evaluated during the first iteration and subsequent iterations require minimal computational effort. We note that this iterative technique offers an n_c^2 increase in computational efficiency.

The convergence rate can be significantly improved by using the latest estimate for $\overline{\psi}^{LMS\Pi}_{i,l_1^{a'} l_2^{a'},b+1}(r_1, r_2)$ as soon as it becomes available. Unfortunately, as with the ECS/CGS iterative method, iterative coupling of the PECS equations gives diverging solutions at low energies, due to very strong electron correlation. It is possible, however, to reach lower total energies by fully-coupling groups of partial waves, and iteratively coupling the separate groups. For example, if n_c coupled $\left|LMS\Pi l_1^a, l_2^a\right\rangle$ partial waves are required for convergence of $|LMS\Pi\rangle$, we can order these into n_g groups (or sets) such that $\sum_{g=1}^{n_g} n(g) = n_c$, where $n(g)$ gives the number of separate (l_1, l_2) in each group g. The iteratively coupled Schrödinger equation becomes

$$\left(2E + \frac{\partial^2}{\partial r_1^2} + \frac{2Z}{r_1} - \frac{l_1^a\left(l_1^a+1\right)}{r_1^2} + \frac{\partial^2}{\partial r_2^2} + \frac{2Z}{r_2} - \frac{l_2^a\left(l_2^a+1\right)}{r_2^2}\right) \overline{\psi}^{LMS\Pi}_{i,l_1^a l_2^a,b+1}(r_1, r_2) - 2\sum_{a' \in g} \left\langle l_1^a l_2^a \middle\| \frac{1}{r_{12}} \middle\| l_1^{a'} l_2^{a'} \right\rangle_L \overline{\psi}^{LMS\Pi}_{i,l_1^a l_2^a,b+1}(r_1, r_2) = \overline{\xi}^{LMS\Pi}_{i,l_1^a l_2^a,b+1}(r_1, r_2), \tag{58}$$

where

$$\overline{\xi}^{LMS\Pi}_{i,l_1^a l_2^a,b+1}(r_1,r_2) = \chi^{LMS\Pi}_{i,l_1^a l_2^a}(r_1,r_2) + 2\sum_{\substack{a'<a\\ a'\notin g}} \left\langle l_1^a l_2^a \right\| \frac{1}{r_{12}} \left\| l_1^{a'} l_2^{a'} \right\rangle_L \overline{\psi}^{LMS\Pi}_{i,l_1^{a'} l_2^{a'},b+1}(r_1,r_2)$$

$$+ 2\sum_{\substack{a''>a\\ a''\notin g}} \left\langle l_1^a l_2^a \right\| \frac{1}{r_{12}} \left\| l_1^{a''} l_2^{a''} \right\rangle_L \overline{\psi}^{LMS\Pi}_{i,l_1^{a''} l_2^{a''},b}(r_1,r_2), \tag{59}$$

and where $\in$ and $\notin$ have their standard set notation meaning and for each iteration we assume that wavefunctions are calculated sequentially, in ascending order of a. The grouping and iterative coupling of partial waves in this manner is used when iterative convergence becomes marginal, and is also used to satisfy the requirement that $\left(l_1^a, l_2^a\right)$ and $\left(l_2^a, l_1^a\right)$ are solved simultaneously, and hence fully coupled. Assuming that the size of each group is the same, the increase in computational efficiency of this coupling method compared with the fully-coupled solution is approximately n_g^2.

It is worth noting that though this iterative-coupling method was conceived independently, based upon computational features of the PECS method, it is similar to an iterative technique used successfully by Allison [57] for one-dimensional Schrödinger equation problems.

3.5. Energy perturbation method

The PECS iterative coupling technique provides a dramatic improvement in computational efficiency, though fails to converge for energies close to ionization threshold. Another iterative refinement technique that *does* converge over a broad range of energies, including near threshold, allows us to efficiently calculate scattering wavefunctions for many finely spaced energies. This energy-perturbation method may also be used in combination with the iterative coupling technique described in the previous section if iterative coupling alone provides convergent solutions.

After evaluating the scattering wavefunctions for total energy E we can iteratively approximate the scattering wavefunctions for energy $E' = E + \Delta E$ using (58), where

$$\overline{\xi}^{LMS\Pi}_{i,l_1^a l_2^a,b+1}(r_1,r_2) = \chi^{LMS\Pi}_{i,l_1^a l_2^a}(r_1,r_2) + 2\sum_{\substack{a'<a\\ a'\notin g}} \left\langle l_1^a l_2^a \right\| \frac{1}{r_{12}} \left\| l_1^{a'} l_2^{a'} \right\rangle_L \overline{\psi}^{LMS\Pi}_{i,l_1^{a'} l_2^{a'},b+1}(r_1,r_2)$$

$$+ 2\sum_{\substack{a''>a\\ a''\notin g}} \left\langle l_1^a l_2^a \right\| \frac{1}{r_{12}} \left\| l_1^{a''} l_2^{a''} \right\rangle_L \overline{\psi}^{LMS\Pi}_{i,l_1^{a''} l_2^{a''},b}(r_1,r_2) - 2\Delta E \overline{\psi}^{LMS\Pi}_{i,l_1^a l_2^a,b}(r_1,r_2), \tag{60}$$

and begin the iteration by equating $\overline{\psi}^{LMS\Pi}_{i,l_1^a l_2^a,0}$ to the scattering wave solution for energy E. As the left-hand side of (58) is unchanged from the evaluation of energy E, the same $\boldsymbol{A}^{(i)}$, $\boldsymbol{B}^{(i)}$, $\boldsymbol{C}^{(i)}$ and $\boldsymbol{D}^{(i)}$ matrices are used to evaluate energy E' and no additional matrix inversions are required. Consequently, scattering wavefunctions can be evaluated for many closely spaced energies with minimal computational resources. The grid spacing, R_0, $R_{\max}$ and the coupled angular-momentum states must be selected to provide good convergence at both E and E'. This method is used extensively in later sections to investigate the resonance structure of scattering collisions below the ionization threshold and the threshold behaviour of e–H ionizing collisions.

When non-iterative solutions are used ($n_g = 1$ and $\Delta E = 0$) there is little computational advantage in maintaining the $\tilde{\boldsymbol{B}}^{(i)}$ matrices in memory. To minimize hard disk requirements for very large calculations $\tilde{\boldsymbol{B}}^{(i)}$ and $\vec{\boldsymbol{E}}^{(i)}$ can be written to disk for only certain milestone values

of i (when the available memory fills) during the forward pass of the propagation algorithm (evaluating (51)–(53)). Then, on the backward pass (evaluating (49)), the milestones are read from disk and all matrices between the milestone values of i are recalculated. Though this results in an overall doubling of computation time, it allows very large grids to be evaluated without significant restrictions being imposed by either computer memory or hard-disk capacity.

4. Convergence study

The PECS method uses *numerical approximation* techniques, rather than analytic methods, to solve the Schrödinger equation for e–H collisions. Also, the integral methods used to extract scattering and ionization amplitudes from the scattering wavefunction rely upon *asymptotic approximations*. It is important, therefore, that errors introduced into the calculations by these approximations are controlled so that the standard error of the calculations can be estimated. These approximations can be divided into four broad categories: grid spacing and complex scaling, grid size, iterative coupling and partial-wave expansion. We will now investigate the convergence behaviour of each of these approximations, where it will become evident that the convergence of the PECS calculations is very stable and predictable, and capable of very high accuracy.

4.1. Grid spacing and complex scaling

The accuracy of the Numerov formulae (B.2) increases with smaller grid spacing, and in general, finer spacing is required near the nucleus where the electrostatic potential can be very large. However, the computational requirements increase rapidly with finer grids and a balance must be sought between the required accuracy and the available computational resources. In this section, we investigate convergence w.r.t. grid spacing of the singlet ($S = 0$) s-wave model (where only one partial wave $L = l_1 = l_2 = 0$ is solved) at $E_0 = 27.2$ eV. Convergence of this model is representative of the full e–H calculations.

The exact solutions for the s-wave model are not known, so the error estimates given are relative to a very fine reference grid with six separate grid-spacing regions, shown in table 2. The start, length and number of regions are somewhat arbitrarily selected and can be changed, but each change would require a separate convergence study. The selected regions, however, have proven to be computationally efficient and are sufficient for the purpose of investigating grid-related convergence issues.

The relationship between the magnitude of the relative error in the TICS and the grid spacing in each region is shown in figure 4(a). Some interesting conclusions can be drawn from these results.

The results show an approximate power-law relationship between estimated error and grid spacing, though the h_1 and h_2 regions have a different slope (and hence power law) to the remaining regions. The approximate relationships for the example grid and kinematics are: for $n = 1, 2$ the error is approximately $a_n h_n^2$ and for $n = 3, 4, 6$ is approximately $a_n h_n^4$, where a_n is a constant of proportionality. Note that these estimates are the combined errors from the two-dimensional variable-grid Numerov formula, two-dimensional Chebyshev-polynomial grid interpolation and the sensitivity of the Peterkop integral equations to errors in various regions of the grid, and cannot be directly related to the theoretical error of the Numerov formulae given in (47).

Also, the results conclusively demonstrate that finer grid spacing is required in the inner regions of the grid, and may be increased with increasing r. The plot also shows an instability

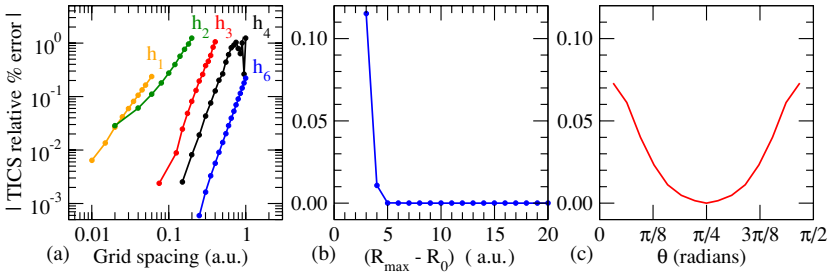

Figure 4. Relative percentage error of the TICS for (a) varying grid spacing in each grid region h_n (excluding h_5), (b) complex scaling length ($R_{\max} - R_0$) with fixed $\theta = \pi/4$ rad, and (c) complex scaling angle θ. All results are calculated for the singlet s-wave model at $E_0 = 27.2$ eV, $R_0 = 200$ au and errors are relative to the reference-grid calculation in table 2.

Table 2. Grid spacing regions used for convergence testing of the PECS s-wave model at $E_0 = 27.2$ eV with $R_0 = 200$ au and $\theta = 0.8$ rad. Measurements are along the real axis, except h_6 is measured along the complex contour. The converged grid column represents the maximum grid spacing able to maintain a standard error of 0.2% in the TICS.

			Grid spacing h_n (au)	
Region (n)	Start (au)	Length (au)	Reference grid	Converged grid
1	0.0	0.2	0.005	0.02
2	0.2	1.8	0.005	0.06
3	2.0	18.0	0.050	0.20
4	20.0	180.0	0.100	0.40
5	200.0	2.0	0.005	0.10
6	202.0	18.0	0.200	0.70
TICS (au)			0.06721	0.06734
1s–1s ICS (au)			0.4117	0.4111

for $h_4 > 0.7$, which gives an upper limit to the grid spacing in the real region of the grid at this energy.

We also found that the inner grid spacings h_1 and h_2 are relatively insensitive to the energy of the incident electron, but vary as a function Z (the charge on the nucleus) and the initial state of the target. The grid spacing in the outer regions *is* influenced by the energy of the incident electron, and we can readily estimate the relationship between them. If we consider the outer regions of the scattering wavefunction, the most oscillatory area corresponds to elastic scattering ($r_1 \ll r_2$ or $r_1 \gg r_2$), where the scattered electron has maximum energy (E_0) and maximum momentum ($\sqrt{2E_0}$). The wavelength of the scattering wavefunction in this region will be inversely proportional to the momentum. The number of grid points per oscillation should be maintained when E_0 is varied, thus to maintain 0.1% accuracy $h_4 \approx 0.4/\sqrt{E_0}$ is needed (using au). The energy scaling of h_6 can be obtained in a similar way, and $h_3 \approx (h_2 + h_4)/2$ gives a rough estimate for the transition region.

The relationship between grid spacing and incident-electron energy is only a rough approximation and many other factors (especially R_0) will influence the final error estimate. Interestingly, the errors of the ionization and scattering cross sections (not shown) demonstrate a similar dependence on the grid spacing in each region, even though the major contribution to

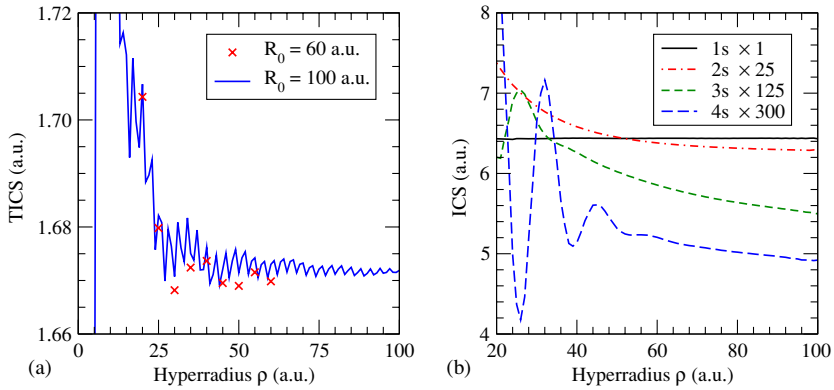

Figure 5. Convergence of e–H total cross sections w.r.t. hyperradius ρ for (a) ionization at $E_0 = 27.2$ eV ($L \leqslant 12$, $R_0 = 60$ and 100 au), and (b) discrete final-state scattering at $E_0 = 30.0$ eV ($L \leqslant 50$, $R_0 = 100$ au).

each comes from different regions of the scattering wavefunction: the dominant contribution to ionization comes from the region where both r_1 and r_2 are large (h_4 region), whereas the dominant contribution to elastic scattering is in the region where one of r_1 or r_2 is small (h_1 and h_2 region). From this we can infer that errors introduced by the spacing in one region affect the accuracy of the scattering wavefunction in other regions.

The effect of grid spacing near R_0 is more difficult to analyse, as the error varies in different regions of the grid depending on the 'sharpness' of the discontinuity in the first derivative of the scattering wavefunction at R_0 (see figure 1). See [32] for a detailed discussion on the errors in this region.

Figures 4(b) and (c) show the relative error in TICS w.r.t. complex scaling length and angle of rotation. Provided that the region of complex scaling ($R_{\max} - R_0$) gives sufficient exponential damping of the outgoing scattering wavefunction, we have found that the angle of rotation into the complex plane and the complex scaling length of the radial coordinates has negligible effect on the ionization and scattering cross section calculations. This is consistent with the results of Baertschy *et al* [48]. At $E_0 = 27$ eV the relative error when $R_{\max} - R_0 = 5$ au is negligible, and beyond 7 au the TICS remains constant to six significant figures. At this impact energy, this complex scaling length represents approximately one oscillation of the scattering wavefunction. Using this criterion, we can estimate the scaling length using $R_{\max} - R_0 \gtrsim 5.0/\sqrt{2E}$, when $\theta \approx \pi/4$.

4.2. Grid size (R_0) and hyperradius (ρ)

The surface integral methods used to extract cross sections from the scattering wavefunctions [(24) and (34)] depend upon asymptotic approximations for the final-state continuum waves, and will therefore exhibit an error that diminishes with the increasing (hyper)radius. This is generally the largest component of the overall error and it is important to investigate this convergence for each calculation.

The radial convergence of e–H TICS and discrete final-state cross sections at $E_0 = 27.2$ eV are presented in figure 5. There is excellent agreement between the $R_0 = 60$ au and 100 au TICS results at the same ρ, which indicates that R_0 has a little effect on the accuracy of the scattering wavefunction. The diminishing ρ-dependent oscillations in the ionization cross section are consistent with formal theory [50, 51] and the TICS demonstrates

excellent convergence at 100 au, with oscillations of the order of $\pm 0.05\%$. The ρ required for convergence varies inversely with total energy E.

The smoothed $0 < \rho \leqslant R_0$ results can be extrapolated to estimate the asymptotic TICS. This, in addition to the error estimate from the grid-spacing convergence tests, is used to estimate the total standard error of the calculation. None of the ionization results undertaken with PECS are based on a radial extrapolation of the cross sections, but are made at sufficiently large R_0 that they are effectively converged.

The discrete-final-state cross sections presented in figure 5(b) converge in a similar way to the TICS, but without significant (short wavelength) oscillations. Beyond $\rho \approx 4n_j^2$ au, where n_j is the final-state orbital quantum number, the cross sections stabilize and then converge at a rate approximately proportional to $1/\rho$. The elastic cross section is constant to within $\pm 0.05\%$ for $\rho > 20$ au, while excited collisions require increasingly larger ρ. Unless stated otherwise, we generally do not extrapolate ICS or DCS results, w.r.t. ρ, but do use it to estimate the error of the results presented.

The cross sections for charged hydrogenic targets and excited-state targets converge in a similar way to these H(1s) results.

4.3. Iterative coupling and energy perturbation

The single largest improvement in the computational efficiency of PECS is obtained from the iterative coupling and energy perturbation techniques. However, these techniques are not convergent for all calculations. Here we investigate the collision and computational parameters that influence convergence.

The rate that the PECS iterative-coupling technique converges can be seen in figure 6(a) for an e–H collision at $E_0 = 27$ eV. The trend of these partial waves is representative of other partial waves. Two significant features of the iterative coupling technique can be observed in this plot. Firstly, once a converging trend is demonstrated for all coupled partial waves ($b \geqslant 8$ in this example), the error of the partial cross sections ($\sigma_{0,0}$ and $\sigma_{5,5}$) are closely matched by the maximum relative change in their associated scattering wavefunctions ($\psi_{0,0}$ and $\psi_{5,5}$). As the ionization cross section calculations are much more computationally intensive than a simple difference calculation, the contribution of iterative coupling to the TICS error can be estimated at each iteration without incurring a large computational overhead. Throughout this tutorial iterative coupling is continued until *all* partial waves converge to better than 0.1%. Secondly, the states with the largest contributions to the TICS are the first to converge, and will therefore be converged to a much greater accuracy. In this example, $(l_1, l_2) = (5, 5)$ has converged to better than 0.1% by $b = 20$ at which point the *total* cross section for $L = 0$ $S = 0$ has converged to within 0.0001% of the fully-coupled solution. As such, iterative coupling has a negligible contribution to the estimated error.

The iterative coupling convergence rate is different for each spin state and is strongly related to the energy of the incident electron. In figure 6(b), we see that the number of iterations required to achieve convergence increases rapidly with decreasing total energy. At energies near the ionization threshold, the iterative coupling technique becomes divergent. The triplet spin state, by comparison, requires much fewer iterations and does not become divergent until the energy is very close to ionization threshold. Though the $L = 0$ triplet wavefunction in this example becomes increasingly suppressed as the energy approaches zero, due to the Pauli exclusion principle, the convergence rate for *all* triplet states is similar. Likewise, when the target is initially in an excited state with $l_i \geqslant 1$ (when odd parity is allowed) the odd parity states (both singlet and triplet) converge much more quickly than even parity states.

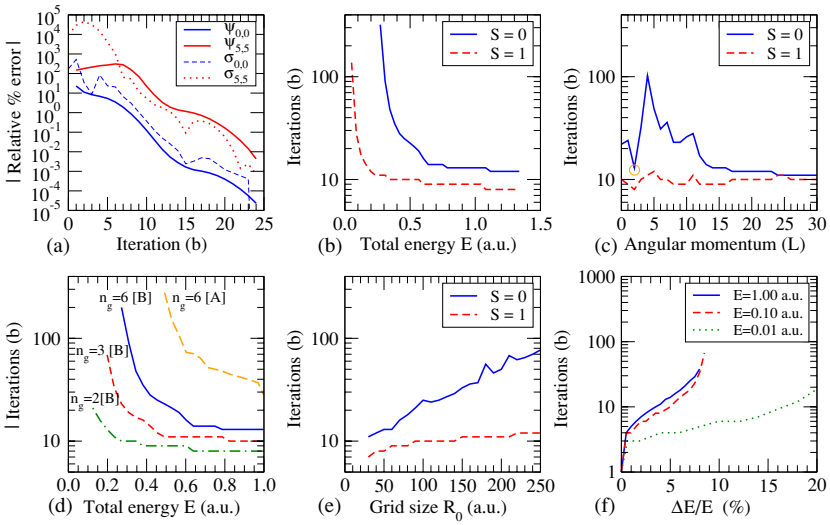

Figure 6. e–H iterative-convergence study. (a) Error relative to fully-coupled ($n_g = 1$) calculation of scattering wavefunction and partial TICS ($L = S = 0$; $E_0 = 27$ eV; $l_1, l_2 = 0, 0$ and 5, 5) with increasing iteration number. (b)–(e) Iterative coupling iterations required for convergence of the TICS to better than 0.1%, w.r.t. increasing: (b) total energy ($L = 0$), (c) angular momentum L at $E_0 = 27$ eV (using maximum n_g except circled datum), (d) total energy for $L = S = 0$ using different number of coupling groups (n_g) and methods (A, B), and (e) grid size at $E_0 = 27$ eV ($L = 0$). (f) Energy-perturbation iterations required to converge $L = S = 0$ scattering wavefunction (to better than 0.01%) for varying $\Delta E/E$ at $E = 1.00$, 0.10 and 0.01 au, using $R_0 = 70$, 100 and 200 au, respectively, and $n_g = 1$.

The rate of convergence of the iterative coupling technique is also dependent upon the angular momentum L of the partial wave. Generally, the L that has the largest contribution to the TICS requires the most iterations. The results for $E_0 = 27$ eV are shown in figure 6(c), noting that for $L = 2$ (which provides the largest contribution to the TICS) a smaller value of n_g was required to achieve an acceptable convergence rate. Convergence for higher L and all triplet states was rapid.

In figure 6(d), we see that using the latest iterative estimate for the coupled partial waves (method [B] using (58)) converges more quickly than when only the results of the previous iteration are used (method [A] using (56)), and is convergent to much lower total energies. The convergence rate of method [B] can be further improved, and used at energies closer to ionization threshold, by reducing the number of iterative-coupling groups n_g. However, this also increases the memory requirement and calculation time. Figure 6(e) shows that the number of iterations increases with increasing grid size. When convergence of the PECS iterative coupling technique becomes marginal or diverges, there are several strategies in addition to decreasing n_g that improve the rate of convergence. These are discussed in [32].

Unlike iterative coupling, the energy perturbation method is convergent over a broad range of energies, including those near and below ionization threshold. Figure 6(f) shows the range of $\Delta E/E$ for which convergent results can be obtained, for several total energies. Generally, good convergence is obtained for perturbations in *total* energy of $\pm 5\%$, and if iterative-coupling is convergent at the desired energy, both iterative-coupling and energy perturbation iterations can be used simultaneously. Though the range of $\Delta E/E$ for the $E = 0.01$ au calculations is significantly larger, it should be noted that the R_0 used at this energy would not provide TICS results converged to the same accuracy as the other energies.

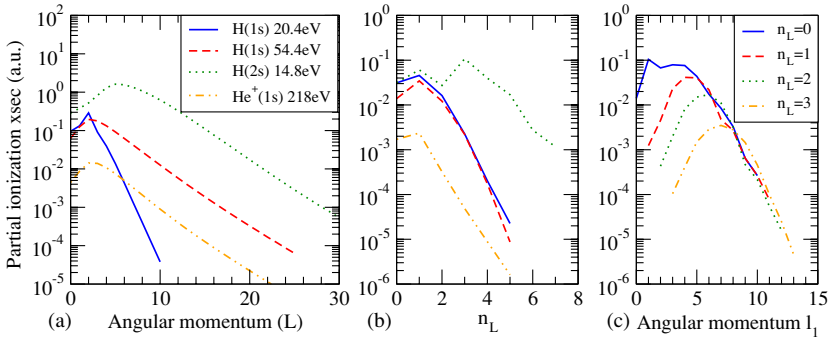

Figure 7. (a) Singlet partial ionization cross sections, w.r.t. L, for various targets and incident-electron energies. (b) Singlet partial ionization cross sections w.r.t. n_L groups of angular-momentum states for $L = 0$ (same targets and legend as (a)). (c) Contribution of (l_1, l_2) angular-momentum states, grouped by n_L, to the $L = 10$ singlet ionization cross section for an H(2s) target at $E_0 = 14.8$ eV.

A relatively large number of iterations are required to achieve convergence for some partial waves with the PECS method, but the computational effort required for each iteration is extremely small. Overall, we estimate that iterative coupling provides a 100-fold reduction in computational effort for e–H calculations at intermediate energies, compared with solutions obtained without iterative coupling. This improvement increases dramatically at higher energies when more partial waves are required.

4.4. Partial-wave expansion

The partial-wave expansion (8) used in the PECS method expands the scattering wavefunction of the collision into an *infinite* sum of LMl_1l_2 partial-wave scattering wavefunctions, where each $LMS\Pi$ can be solved independently. In practice, accurate results are obtained with a relatively small set of partial waves, though this varies considerably with the target state and charge and the incident electron energy.

The L partial-wave contributions to the singlet ionization cross sections of various targets are presented in figure 7(a). For H(1s), the peak contribution is from $L = 2$ (for the energies presented), with an exponential decay with increasing L. The slope of this decay reduces with increasing energy, and consequently higher-energy collisions require more partial waves to maintain similar accuracy. The smoothness of the decay allows the error introduced by truncating the infinite sum to be easily estimated. For $E_0 = 14.8$ eV ionization of H(2s), the peak occurs considerably higher at $L = 5$ and exhibits a similar decay slope to that of $E_0 =$ 54.4 eV H(1s). The impact energies of both collisions are approximately the same number of threshold units (one threshold unit, t.u., is defined as the ionization energy of the target). The peak cross section for $E_0 = 217.7$ eV ionization of $He^+(1s)$ occurs at $L = 2$ and has a similar decay slope as the H($n_i s$) collisions at the same number of threshold units. This peak-L and decay-slope trend is consistent for all calculations undertaken.

The energy dependence and L-decay for the partial *scattering* cross sections is similar to these ionization results, with the exception of elastic scattering which has an increasingly slower decay as L increases, thus requiring more partial waves for convergence. Though the ICS can be calculated accurately with a similar number of partial waves as the TICS, accurate

DCS for discrete final-state collisions requires a much larger set of partial waves to achieve good convergence.

In addition to truncating the L series of the partial-wave expansion, for large L it becomes necessary to truncate the number of coupled (l_1, l_2) states for each L. In the PECS method we have chosen to group these states by the parameter $n_L = (l_1 + l_2 - L - \Pi)/2$. Figure 7(b) shows the partial ionization cross sections w.r.t. n_L for the $L = 0$ singlet partial waves of various targets. The shape of the distribution is similar for all 1s targets, which exhibits a rapid exponential decay with increasing n_L, while the decay for the H(2s) target is significantly slower, and thus requires many more (l_1, l_2) partial waves to achieve good convergence. The peak contribution for ionization is from $n_L = 1$ for ground-state targets and $n_L = 3$ for H(2s). The general trend exhibited by all targets is that as L is increased, the rate of decay w.r.t. n_L increases and convergence can be achieved to the desired accuracy with fewer n_L groups.

The number of (l_1, l_2) for each n_L equals $L + 1$, and it becomes necessary to truncate this series for large L so as to minimize the computational resources needed for the calculations. As an example, we have shown the contribution of each (l_1, l_2) to the $L = 10$ ionization cross section of H(2s) at $E_0 = 14.8$ eV in figure 7(c), grouped by n_L. The shape of the distribution of the partial ionization cross sections is similar for all targets and all n_L, and demonstrates a rapid exponential decay beyond the peak. Though the relative contribution of partial waves with small l_1 is also small, truncating small-l_1 partial-waves severely impacts the remaining partial waves. Only terms beyond the peak can be truncated. Also, as the present PECS method evaluates the scattering wavefunction using a triangular grid, both (l_1, l_2) and (l_2, l_1) states *must* be included. This limits the states that can be truncated to those where both (l_1, l_2) and (l_2, l_1) are well beyond the peak, which generally does not occur until $L \geqslant 12$ for $n_i = 1$ targets and $L \geqslant 18$ for $n_i = 2$ targets, for the energies considered in these examples.

The error introduced by truncating the number of terms in the partial-wave expansion has been estimated by extrapolating the observed decay rate of the series w.r.t. L, n_L and l_1. For all e–H(1s) targets, the contribution to the total estimated error of the TICS introduced by this truncation was maintained at less than 0.05% throughout all calculations presented in this tutorial, and increased to 0.3% for the charged and excited state target calculations. For example, to achieve this accuracy the $E_0 = 27.2$ eV ground-state ionization calculations included $L \leqslant 12$ and the number of coupled (l_1, l_2) ranged between 6 and 32 for each L. The largest calculation undertaken was the H(2p) target at $E_0 = 14.8$ eV, which included $L \leqslant 25$ for singlet and triplet, $M = 0$ and $M = 1$ and both even and odd parities; totalling 152 separate calculations. The number of coupled (l_1, l_2) ranged between 8 and 60 for each calculation, giving a total of 6460 partial-wave scattering wavefunctions.

This completes our investigation of the convergence of PECS for e–H collisions. It is clear from this analysis that PECS can obtain results converged to a very high accuracy. Moreover, the iterative-coupling technique demonstrates an almost linear increase in computation time w.r.t. the number of coupled states. This has facilitated full Schrödinger equation calculations at very-low and high impact-energies as well as excited initial-state collisions.

5. Results

For hydrogen targets, the ECS method has thus far been applied to ground-state ionizing collisions for electron-impact energies in the range 14.6 to 54.4 eV [23, 58, 59]. These calculations were highly accurate and consistent with measurements and other state-of-the-art computational methods. In this section, we present PECS calculations for a *complete* range of electron–hydrogen collisions by considering discrete final-state collisions, both above and

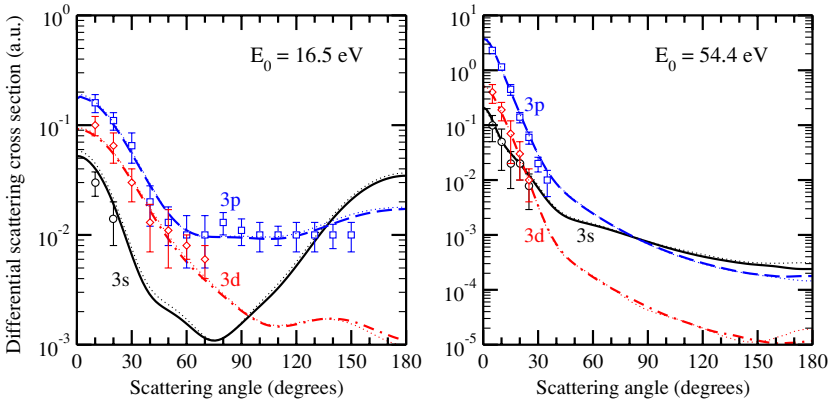

Figure 8. PECS differential scattering cross sections for e–H(1s) 3s, 3p and 3d transitions at $E_0 =$ 16.5 and 54.4 eV. CCC results shown with dotted black lines. Experiment and CCC results from Williams *et al* [41].

below ionization threshold, ionizing collisions over a wide range of energies and electron collisions with excited-state and charged hydrogenic targets.

During this PhD project, and prior to evaluating the full e–H problem, several detailed computational studies using the Temkin–Poet [60, 61] and collinear [62, 63] model potentials were undertaken using the PECS method. These simplified potentials greatly reduce the computational effort by limiting the calculation to a single partial wave and, while not representative of the full e–H problem, provide a rigorous test of the computational and theoretical methods. These scattering, ionization and threshold-law calculations have not been included in this tutorial and interested readers should refer to the relevant publications [33–35].

5.1. Ground-state hydrogen scattering

Our first PECS e–H scattering calculations [36] were undertaken above the ionization threshold at $E_0 = 30$ eV. These differential scattering cross sections for separate final-state orbital angular momenta ($n_j \leqslant 4$) demonstrated excellent agreement with measurements and CCC calculations. Similar agreement with CCC for the constituent angular-momentum states was shown in [32], but at that time l_j-resolved measurements for $n_j \geqslant 3$ were not available.

Recently, Williams *et al* [41] presented the first measurements of e–H(1s) DCS for transitions to the 3s, 3p and 3d final states. We have reproduced these measurements for $E_0 =$ 16.5 eV and 54.4 eV in figure 8, which matched our PECS calculations within experimental error. PECS and CCC also agree very well.

While the partial-wave scattering cross sections for $L > 20$ do not contribute significantly to the *total* scattering cross section of these calculations, their inclusion is required to converge the DCS at small scattering angles and remove oscillations at large backward scattering angles. Scattering amplitudes for partial waves $20 < L \leqslant 200$ were included in our calculations by extrapolating the $L \leqslant 20$ results. This technique is used for all differential *scattering* cross sections presented in this tutorial.

These results give strong evidence of the accuracy of the PECS method for calculating scattering amplitudes. However, the reduced Stokes parameters for the 1s–2p transition provides a more stringent test of our method since they additionally contain information

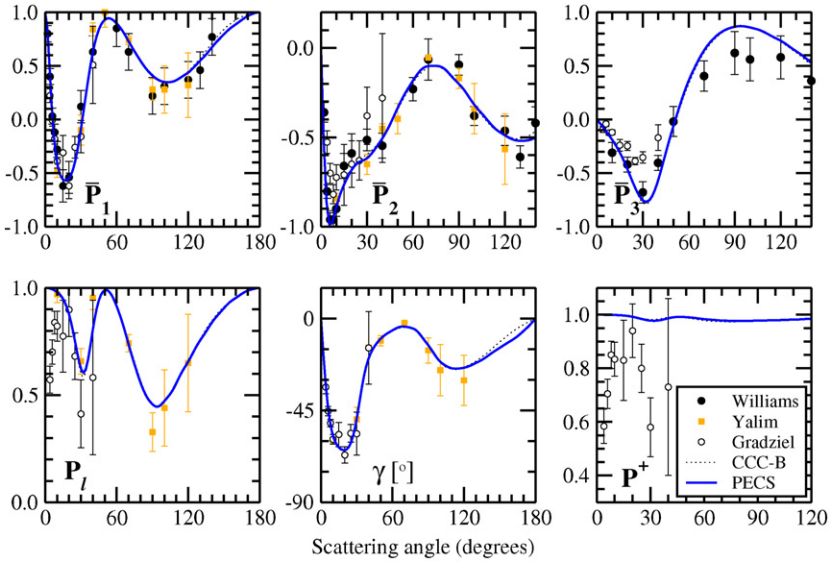

Figure 9. PECS reduced Stokes parameters $\bar{P}_1$, $\bar{P}_2$ and $\bar{P}_3$ and related parameters P_l, γ and P^+ for e–H 1s–2p scattering at $E_0 = 54.4$ eV. CCC box-based calculations (CCC-B) [40] and measurements of Yalim *et al* [65], Gradziel and O'Neill [64] and Williams and Mikosza [66] are also shown.

about the phase of the magnetic sub-level amplitudes, whereas the cross sections only provide information on the magnitude of these amplitudes. In a recent paper, Gradziel and O'Neill [64] presented measurements of $\bar{P}_3$ for electron–hydrogen collisions at 54.4 eV impact energy that disagreed with long-standing CCC calculations [9] and showed structure in the P^+ parameter. The reasons for this apparent discrepancy for e–H collisions were not clear.

In figure 9, we reproduce our results for the reduced Stokes parameters for electron–hydrogen 1s–2p scattering collisions at 54.4 eV from [40], and additionally include the related parameters P_l, γ and P^+. The PECS calculations are almost indistinguishable from the recent CCC-B (box based) results and the $\bar{P}_1$, $\bar{P}_2$, P_l and γ parameters are in excellent accord with the experimental results of Yalim *et al* [65], which have significantly smaller standard errors than Gradziel and O'Neill's measurements. We have limited the scattering angle range of the $\bar{P}_2$ and $\bar{P}_3$ plots to give emphasis to the experimental points; PECS and CCC-B results show similar agreement in the remaining region. Gradziel and O'Neill stated that the accuracy of their measurements for $\theta \leqslant 10^\circ$ were open to question due to finite volume and solid angle effects, which leaves only the 20–30° $\bar{P}_3$ data points that deviate significantly from theory. The close agreement of PECS with CCC calculations for $\bar{P}_3$ gave strong support for these theoretical calculations, especially considering their markedly different methodologies. This suggested that the discrepancy lies with the experimental procedure used by Gradziel and O'Neill [64]. Recent independent measurements of Williams and Mikosza [66] support this conclusion and are now in good agreement with theory.

In the back-scattering region, the coherent summation of the partial-wave scattering amplitudes generally causes the small-L partial waves (with largest magnitude) to cancel and is highly sensitive to the phase of these amplitudes. This often results in small oscillations at $\theta > 150^\circ$ if the cross sections are much smaller than the forward-scattering region, but is generally of little significance. However, the reduced Stokes parameters are calculated from

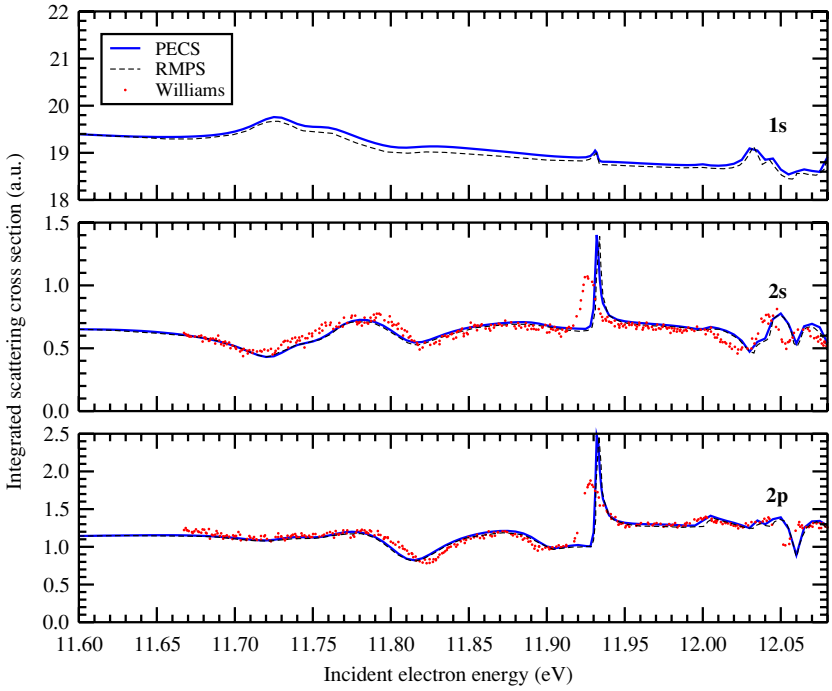

Figure 10. PECS integrated scattering cross section for e–H(1s) 1s, 2s and 2p transitions in the range $E_0 = 11.6$–12.08 eV. RMPS calculations of Bartschat *et al* [67] and measurements of Williams [68] are also shown.

ratios of cross sections and these fluctuations can cause very large ρ-dependent deviations in the Stokes parameters at $\theta \geqslant 150^\circ$. Further investigation revealed that the ρ-dependent oscillations had a wavelength of $\rho_\lambda = \frac{\pi}{k_j}$, and can easily be removed by averaging the results from several ρ over this region.

Finally, to demonstrate the suitability of PECS for calculations below the ionization threshold, we present scattering cross sections for energies in the range $E_0 = 11.6$–12.08 eV, where there are numerous resonance structures. Our results are shown in figure 10 along with the benchmark RMPS calculations of Bartschat *et al* [67] (which matched both CCC and IERM calculations) and the measurements of Williams [68]. Our 2s and 2p results are almost indistinguishable from RMPS, and demonstrate remarkable agreement on the energy, width and magnitude of the resonance features, and are in good agreement with experiment.

Our calculations included 97 energy points spaced at 0.005 eV intervals, and several additional points spaced at 0.001 eV intervals near $E_0 = 11.935$ eV to better define the large resonance peak. The energy range chosen is within 1.6 eV of the $n_j = 2$ threshold and large grids of $R_0 = 200$ au were required to achieve convergence to better than 1% for the $n_j = 2$ cross sections. Our calculations included partial waves $L \leqslant 4$. For a large majority of these energy points we were able to use iterative coupling with maximum n_g, which reduced computational effort dramatically. Furthermore, we were able to use our energy perturbation technique to solve energy points within ± 0.05 eV of the initial energy, providing further significant reductions in computational effort. However, near sharp resonance features, iterative coupling fails to converge and the energy perturbation range narrows, but only for the partial wave(s) responsible for the resonance feature. The computational effort required for

Table 3. Total ionization cross sections for e–H(1s) targets. Energy is given in eV, R_0 and cross sections are in au and spin asymmetry is dimensionless. ECS results are from Baertschy *et al* [23].

		PECS			ECS	
E_0	R_0	L_{max}	TICS	A_s	TICS	A_s
13.88	360	5	0.0405	0.536	–	–
17.6	120	8	0.710	0.505	0.71	0.51
30.0	100	15	1.817	0.396	1.81	0.40
54.4	80	25	2.195	0.259	2.21	0.26
150	40	50	1.617	0.116	–	–

these partial waves is increased as separate $n_g = 1$ calculations are required for each energy near the resonance.

This initial investigation into resonance features below the ionization threshold excluded the highly resonant region $E_0 = 12.080$–12.094 eV just below the $n_j = 3$ threshold. We have subsequently applied PECS to $n_j = 3$ collisions [43] up to and including the highly resonant $n_j = 4$ threshold region, with similar success.

5.2. Ground-state hydrogen ionization

We present TICS and spin asymmetry calculations for a broad range of energies in table 3, which compare extremely favourably with ECS calculations [23] where available. The number of L states required for convergence (L_{max}) increases significantly with energy. At 54.4 eV the large computational requirements limited Baertschy *et al*'s calculations to $L \leqslant 13$ and extrapolation procedures were used for higher partial waves. They also noted that insufficient (l_1, l_2) states could be included for each L to obtain complete convergence w.r.t. angular-momentum states. These higher-energy calculations are readily solved with PECS, and rapid convergence of the iterative coupling procedure ensures minimal computing resources are required. Thus, explicit calculation of the higher partial waves and inclusion of sufficient angular-momentum states was possible for energies up to 150 eV. Higher energy calculations are expected to be readily achievable.

Our 13.88 eV calculation was undertaken at limited R_0 and we estimate the standard error of the TICS is 3.5%, with the increased error due solely to insufficient grid size. This error estimate is based upon the convergence behaviour and oscillations of the TICS near R_0. At this energy, we expect convergence to better than 1% would require a grid size approaching 1500 au, which is beyond our current computational resources.

The SDCS results (w.r.t. energy sharing of the outgoing electrons) for several PECS calculations are shown in figure 11. We have included ECS results for 17.6 eV and 30 eV, which are largely indistinguishable from the present results. Both PECS and ECS results at 17.6 eV contain small oscillations in the SDCS, though the PECS oscillations are not readily observed at the scale presented.

We also present CCC SDCS results [69] in figure 11 at $E_0 = 17.6$, 30.0 and 150 eV. It is well known that CCC calculations exhibit unphysical oscillations in the SDCS (see Bray [70]). Though these oscillations are predicted to converge to the true solution given a sufficiently large pseudo-state basis, it has not been computationally achievable at lower energies. This problem is not unique to CCC and is exhibited by other pseudo-state methods such as IERM and RMPS. However, Stelbovics [21] argues that at $E/2$ the CCC ionization amplitudes will converge to half of their real value, regardless of basis size, and exhibit behaviour much the

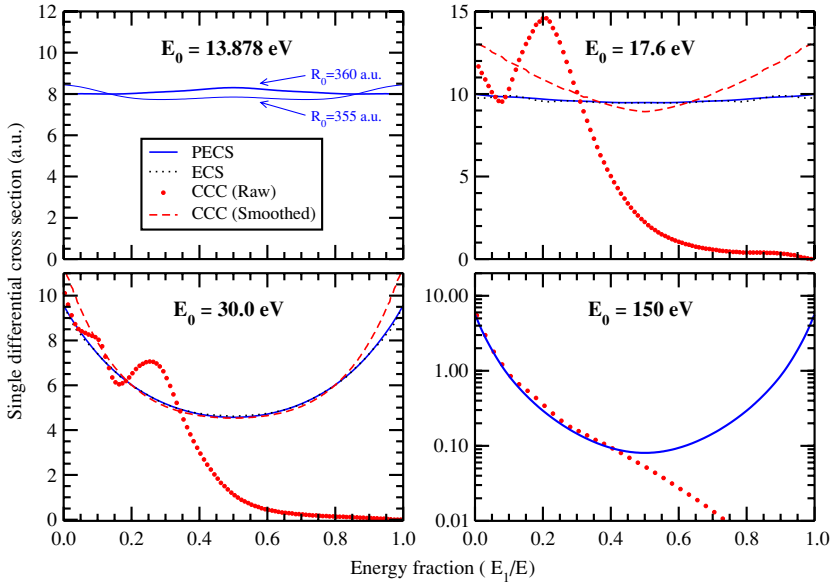

Figure 11. PECS SDCS calculations for e–H(1s) at $E_0 = 13.88$, 17.6, 30.0 and 150 eV. Comparison is made with ECS [23] and CCC [18, 69] calculations. Note that the 150 eV SDCS has steep gradients in the highly asymmetric energy-sharing region and has been plotted with a log scale to help differentiate the curves presented.

same as the truncated Fourier series of a step function, and hence gives $1/4$ of the true cross sections at this point. Hence, the *ab initio* character of the CCC calculations is retained at equal energy-sharing. CCC then constructs a smooth integral-preserving estimate of the SDCS that is four times larger than the raw results at $E/2$. Both the raw and smoothed CCC results are presented. At equal energy-sharing, the 17.6 eV CCC SDCS varies from PECS and ECS results by 5%, which is reasonable considering the difficulty of these low-energy calculations. However, there is a marked deviation in the predicted shape. Given the *ab initio* nature of the PECS and ECS calculations at asymmetric energy-sharing, and the Wannier [29] prediction that the SDCS is nearly independent of electron energy-sharing near threshold, we believe that the shape of the PECS and ECS results provides a better representation of the true SDCS at this energy. At 30 eV, PECS and ECS are in excellent accord and CCC is in better agreement. At 150 eV, where the equal energy-sharing cross sections are relatively small, PECS is in good agreement with the *raw* CCC results for $E_1 \leqslant E_2$.

The 13.88 eV PECS SDCS is given for calculations at $\rho = 355$ and 360 au. This calculation was performed using a restricted grid size, which increases the magnitude of the oscillations of the SDCS. The variation between these results gives an indication of the likely error of the SDCS. The integral of these cross sections varies by 2%, which supports our estimate of the TICS standard error.

Previously [32, 36], we have presented PECS coplanar (where the incident, scattered and ejected electron lie in the same plane) double-differential cross section (DDCS) and triple-differential cross section (TDCS) calculations at 14.6 eV, 17.6 eV, 27.2 eV and 30.0 eV. The results are in excellent agreement with measurements, ECS calculations (where available) and CCC.

In figure 12 we give PECS coplanar TDCS calculations for the moderately-high incident-electron energy of 150 eV. Once again, these results are in very good agreement with CCC

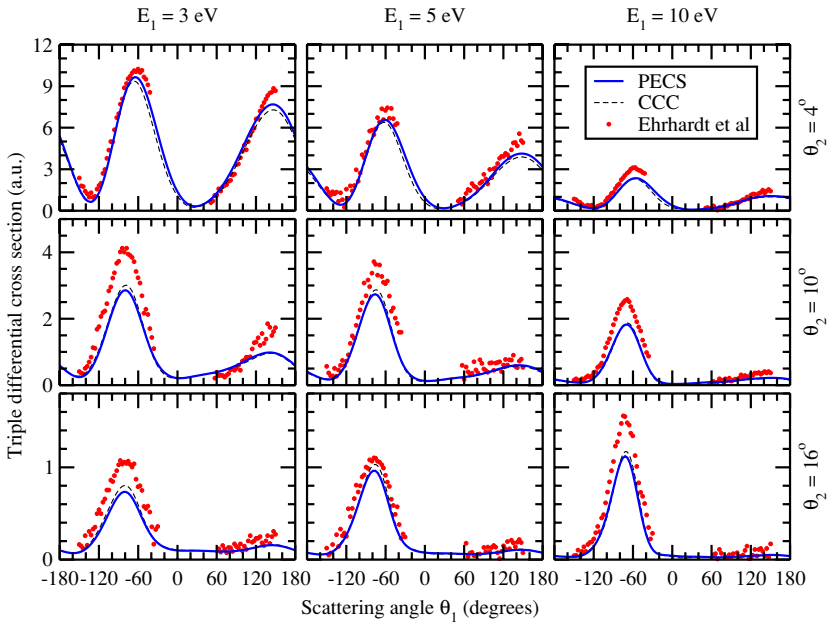

Figure 12. PECS coplanar TDCS calculations for e–H(1s) at $E_0 = 150$ eV. Comparison is made with CCC [18] and absolute measurement [71].

calculations. The position and shape of the peaks agree with the measurements of Ehrhardt *et al* [71], as does the magnitude for kinematics with larger cross sections. There is only moderate agreement with the magnitude of the measured peaks for some kinematics with small cross sections.

Recently [42], we have reported the first study of differential ionization cross sections of e–H collisions in the perpendicular plane, where both outgoing electrons are perpendicular to the incident electron. These are the first out-of-plane calculations and measurements for e–H collisions. The lowest incident energy considered was 14.1 eV, within 0.5 eV of the ionization threshold, and the energies of the DDCS and TDCS outgoing electrons were calculated and measured down to 0.05 eV. The calculations in this publication were in excellent agreement with the new measurements presented, and are further testament to the wide energy range that can be accurately calculated with the PECS method.

5.3. Ground-state hydrogenic ions

The electron-impact scattering and ionization of hydrogenic ions are fundamental to high-temperature plasma modelling, where many highly charged ionic species are present. However, small cross sections and difficulties in preparing suitable target gases makes absolute experimental measurements difficult, especially the differential cross sections. Consequently, there is a heavy reliance upon theoretical calculations. For large nuclear charges Z, the total ionization and scattering cross sections are predicted to scale inversely to Z^4, and the differential ionization cross sections are predicted to scale inversely to Z^6 [72–74]. In this project, we focused on the behaviour of low-Z targets, where the scaling law approximation

Table 4. PECS discrete final-state ICS for ground-state $Z \leqslant 4$ targets, multiplied by Z^4. Energy is in threshold units (t.u.).

		Discrete final-state $(n_j l_j)$scattering cross section $\times Z^4$ (au)									
Z	E (t.u.)	1s	2s	2p	3s	3p	3d	4s	4p	4d	4f
1	0.50	1.04^{+1}	3.12^{-1}	1.87^{+0}	6.36^{-2}	2.83^{-1}	9.28^{-2}	2.42^{-2}	9.42^{-2}	4.71^{-2}	4.50^{-3}
2	0.50	1.23^{+1}	4.54^{-1}	3.14^{+0}	8.50^{-2}	5.03^{-1}	9.03^{-2}	3.14^{-2}	1.70^{-1}	4.59^{-2}	2.70^{-3}
3	0.50	1.22^{+1}	5.44^{-1}	3.66^{+0}	9.95^{-2}	6.04^{-1}	7.93^{-2}	3.67^{-2}	2.10^{-1}	4.03^{-2}	1.91^{-3}
4	0.50	1.20^{+1}	5.97^{-1}	3.92^{+0}	1.11^{-1}	6.60^{-1}	7.44^{-2}	4.11^{-2}	2.33^{-1}	3.75^{-2}	1.58^{-3}
1	1.00	7.27^{+0}	2.62^{-1}	2.11^{+0}	4.69^{-2}	3.29^{-1}	8.18^{-2}	1.77^{-2}	1.12^{-1}	4.11^{-2}	2.57^{-3}
2	1.00	8.24^{+0}	3.85^{-1}	3.16^{+0}	6.89^{-2}	5.15^{-1}	6.80^{-2}	2.54^{-2}	1.79^{-1}	3.30^{-2}	1.34^{-3}
3	1.00	8.16^{+0}	4.50^{-1}	3.54^{+0}	8.26^{-2}	5.90^{-1}	6.09^{-2}	3.00^{-2}	2.06^{-1}	2.96^{-2}	9.98^{-4}
4	1.00	7.97^{+0}	4.88^{-1}	3.73^{+0}	9.15^{-2}	6.28^{-1}	5.82^{-2}	3.33^{-2}	2.21^{-1}	2.79^{-2}	8.38^{-4}
1	3.00	3.02^{+0}	1.95^{-1}	2.26^{+0}	3.58^{-2}	3.67^{-1}	5.45^{-2}	1.30^{-2}	1.28^{-1}	2.43^{-2}	7.68^{-4}
2	3.00	3.18^{+0}	2.53^{-1}	2.80^{+0}	4.79^{-2}	4.62^{-1}	4.23^{-2}	1.76^{-2}	1.63^{-1}	1.94^{-2}	4.56^{-4}
3	3.00	3.15^{+0}	2.77^{-1}	2.95^{+0}	5.32^{-2}	4.95^{-1}	3.92^{-2}	1.96^{-2}	1.74^{-1}	1.82^{-2}	3.86^{-4}
4	3.00	3.11^{+0}	2.89^{-1}	3.03^{+0}	5.59^{-2}	5.07^{-1}	3.84^{-2}	2.06^{-2}	1.79^{-1}	1.79^{-2}	3.60^{-4}
1	5.00	1.81^{+0}	1.59^{-1}	2.05^{+0}	3.05^{-2}	3.41^{-1}	3.49^{-2}	1.12^{-2}	1.19^{-1}	1.61^{-2}	3.91^{-4}
2	5.00	1.86^{+0}	1.87^{-1}	2.37^{+0}	3.59^{-2}	3.98^{-1}	3.09^{-2}	1.32^{-2}	1.41^{-1}	1.44^{-2}	2.86^{-4}
3	5.00	1.84^{+0}	2.00^{-1}	2.45^{+0}	3.91^{-2}	4.12^{-1}	2.82^{-2}	1.45^{-2}	1.45^{-1}	1.33^{-2}	2.49^{-4}
4	5.00	1.83^{+0}	2.06^{-1}	2.49^{+0}	4.03^{-2}	4.19^{-1}	2.80^{-2}	1.49^{-2}	1.48^{-1}	1.32^{-2}	2.41^{-4}

does not rigorously apply, which gave insight into the energies and Z for which the scaling law becomes accurate.

The scattering cross sections for hydrogenic targets with $Z \leqslant 4$ are presented in table 4 for all $n_j l_j$ final states with $n_j \leqslant 4$ at total energies of 0.50, 1.00, 3.00 and 5.00 t.u. The estimated standard error of the results range from 1% for the 1s results to 4% for the 4f results. The results have been multiplied by Z^4 to highlight the convergence behaviour of these cross sections w.r.t. Z and E. For each scaled total energy (t.u.) and final state, the cross sections form a converging series w.r.t. increasing charge Z of the target. The 3d, 4d and 4f final states do not show consistent convergence behaviour at $E = 0.5$ t.u., and calculations for larger Z are required to determine if a converging series is eventually formed for these collisions. The larger estimated error of these calculations may have influenced the apparent non-convergence of these series. Apart from these minor exceptions, the results give strong evidence of a Z^4 scaling of the discrete final-state cross sections at large Z or high energy.

It is evident that the elastic cross sections (1s) converge much more quickly than the excited final-state cross sections, and the convergence rate of all final states increases at higher scaled total energies. The convergence here is consistent with our findings for ionization given in [32, 38], where we analysed the TICS, SDCS, DDCS and TDCS for the same targets and energies. To our knowledge, state-of-the-art methods had not previously been applied to the differential ionization cross sections of these charged targets. Our results now support the Z^4 scaling for both scattering and ionization cross sections, in addition to the Z^6 scaling for ionization differential cross sections. They are also consistent with the experimental analysis of Tinschert *et al* [75] (as discussed in Stia *et al* [74]) that proposes that the scaling laws become valid for $E_0 > (Z/2)^2 \times 500$ eV, and extrapolation of our results will allow accurate predictions for the cross sections of higher Z targets.

Table 5. PECS e–H(2s) and e–H(2p) 14.8 eV discrete final-state integrated scattering cross sections, along with separate M-state contributions for H(2p) targets. CCC results from Bray [69].

	2s initial state		2p initial state			
$n_j l_j$	PECS	CCC	$M = 0$	$M = \pm 1$	PECS	CCC
1s	4.68^{-1}	4.86^{-1}	4.80^{-1}	3.48^{-1}	1.18^{+0}	1.18^{+0}
2s	1.27^{+2}	1.25^{+2}	–	–	–	–
2p	–	–	2.10^{+1}	4.01^{+1}	1.01^{+2}	9.89^{+1}
3s	8.64^{+0}	8.82^{+0}	4.50^{-1}	3.90^{-1}	1.23^{+0}	1.26^{+0}
3p	2.45^{+1}	2.48^{+1}	1.65^{+0}	4.42^{+0}	1.05^{+1}	1.08^{+1}
3d	2.70^{+1}	2.81^{+1}	2.15^{+1}	1.86^{+1}	5.87^{+1}	6.03^{+1}
4s	1.64^{+0}	1.72^{+0}	1.18^{-1}	9.31^{-2}	3.04^{-1}	2.98^{-1}
4p	4.95^{+0}	5.03^{+0}	3.35^{-1}	8.60^{-1}	2.06^{+0}	2.14^{+0}
4d	3.13^{+0}	3.32^{+0}	3.02^{+0}	3.11^{+0}	9.23^{+0}	9.59^{+0}
4f	3.45^{+0}	3.22^{+0}	1.82^{+0}	1.15^{+0}	4.12^{+0}	3.90^{+0}

5.4. Excited-state hydrogen scattering

Scattering and ionization cross sections of excited-state hydrogen targets are also important in plasma modelling as excited atoms are formed in large quantities by the charge-exchange reactions of energetic ions [76]. However, measurement has thus far been limited to the metastable 2s state of hydrogen due to the short lifetime of the other excited states, and only limited state-of-the-art computational results are available. It is evident from our convergence study that collisions with excited-state hydrogen require a much large set of partial waves to achieve convergence, making these problems particularly difficult to solve using partial-wave expansion techniques. To help verify the PECS results presented in this section, Bray [69] has kindly undertaken CCC calculations for comparison.

Ground-state collisions are restricted to $M = 0$ states and even parity, and while electron collisions with H(2s) have the same restrictions, there is no such limitations for H(2p) targets. As such, the e–H(2p) results presented in this section serves as a final test of our PECS equations, derived for targets with arbitrary initial state.

The scattering wavefunctions for electron collisions with H(2s) and H(2p) targets were calculated using an incident energy of 14.8 eV (which has the same total energy as a $E_0 = 25$ eV collision with a ground-state target) and a grid size of $R_0 = 100$ au. Partial waves with $L \leqslant 25$ were required to obtain good convergence of the ionization amplitudes and ICS. The n_L used to achieve convergence w.r.t. angular momentum were $n_L \leqslant 7$ for $L \leqslant 2, n_L \leqslant 6$ for $3 \leqslant L \leqslant 4$, $n_L \leqslant 5$ for $5 \leqslant L \leqslant 7, n_L \leqslant 4$ for $8 \leqslant L \leqslant 9, n_L \leqslant 3$ for $10 \leqslant L \leqslant 14$ and $n_L \leqslant 2$ for $L \geqslant 15$. The odd parity partial waves converged with smaller n_L: $n_L \leqslant 4$ for $L \leqslant 2, n_L \leqslant 3$ for $L \leqslant 7$ and $n_L \leqslant 2$ for $L \geqslant 8$. The estimated standard error of our ICS results ranges from 1% for elastic collisions to 4% for $n_j = 4$ final states.

Results for the electron-impact scattering cross sections for final states $1 \leqslant n_j \leqslant 4$ of both H(2s) and H(2p) targets are presented in table 5 along with CCC results [69], and show good agreement between these methods. The contributions from separate M states are also given for the PECS calculations. The cross sections for 2s–2p and 2p–2s transitions, however, are not given as they are not convergent w.r.t. increasing L. The partial cross sections of our calculations for these transitions diminish approximately at the rate of $1/L$, which gives an infinite cross section if L were extrapolated to infinity. This is an expected outcome as these final states are degenerate in the non-relativistic Schrödinger equation used by the PECS and

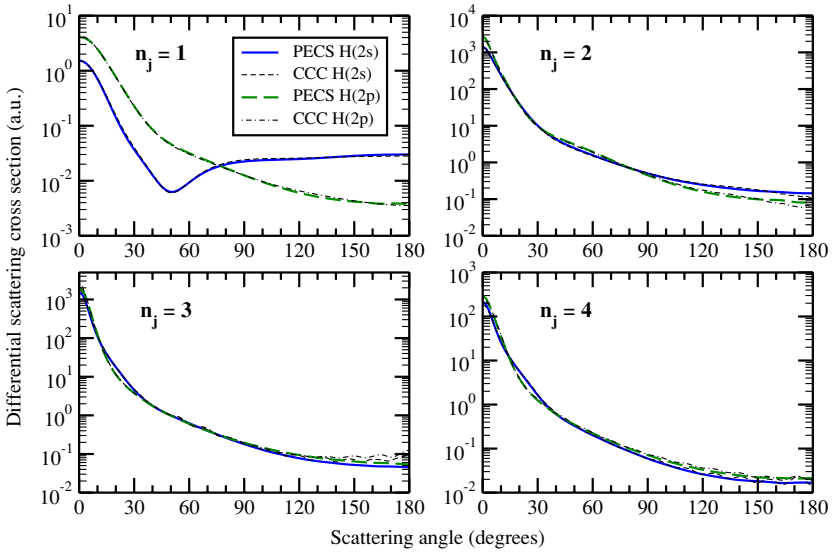

Figure 13. PECS e–H(2s) and e–H(2p) differential scattering cross sections at 14.8 eV for final states $n_j \leqslant 4$. Calculations include partial waves $L \leqslant 25$ and extrapolated partial wave amplitudes for $25 < L \leqslant 200$. CCC results from Bray [69].

CCC methods. To obtain cross sections for these transitions the relativistic Dirac equation must be used, which was beyond the scope of this project.

The differential scattering cross sections for the transitions presented in table 5, summed over l_j, are shown in figure 13. Partial waves $L \leqslant 25$ were included in these calculations, and extrapolated amplitudes were included for $25 < L \leqslant 200$ to smooth the oscillations in the back-scattering region. The results agree with CCC [69] for each $n_j l_j$ state, though to aid clarity only the total n_j cross sections are presented. There are slight variations between PECS and CCC near $\theta = 180^\circ$, though this region is many orders of magnitude smaller than the peak and does not affect the accuracy of the ICS. Importantly, the PECS results remain relatively smooth in this computationally difficult region, which highlights the stability of the phase of the scattering amplitudes.

While the total DCSs for $n_j \geqslant 2$ are very similar for 2s and 2p targets, the separate l_j contributions are very different (see [32]), as is suggested by the ICS results in table 5. The super-elastic DCS results for transitions to the ground state ($n_j = 1$) are also very different for these targets.

5.5. Excited-state hydrogen ionization

The TICS and spin asymmetry for e–H(2s) and e–H(2p) collisions at 14.8 eV presented in table 6 have an estimated standard error of 1%. These results are in good agreement with CCC [69], and agree with experiment [76] for the 2s state (obtained by interpolating measurements at nearby energies) within experimental uncertainty. The SDCS for these collisions are presented in figure 14, along with the separate M-state and parity contributions for the 2p target. The 2s SDCS is in good agreement with CCC, with only minor differences at near equal energy-sharing and highly asymmetric energy-sharing. This difference may be an artefact of the smoothing algorithm used in the CCC method. CCC differential cross sections for the 2p

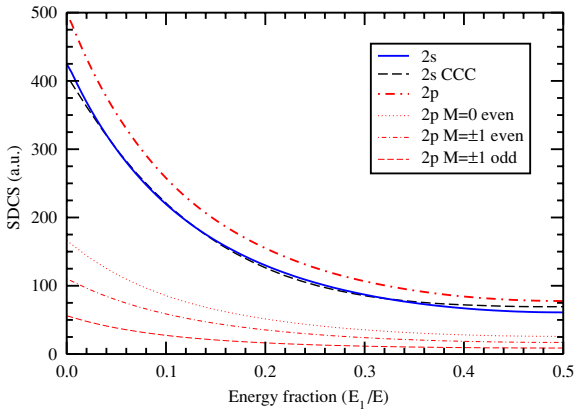

Figure 14. PECS e–H(2s) and e–H(2p) SDCS at 14.8 eV. Calculations include partial waves $L \leqslant 25$. CCC results from Bray [69].

Table 6. PECS e–H(2s) and e–H(2p) 14.8 eV TICS and spin asymmetry results. CCC [69] calculations and experimental [76] results (interpolated) are presented where available. PECS calculations include partial waves $L \leqslant 25$, singlet and triplet results are spin weighted and are given in au.

Method	$n_i l_i$	M	$S = 0$	$S = 1$	Total	A_s
PECS	2s	0	11.9	18.3	30.2	0.191
CCC	2s	0	11.9	18.6	30.5	0.186
Experiment	2s	0	–	–	29 ± 3	–
PECS	2p	0	4.82	7.20	12.0	0.201
PECS	2p	± 1	3.95	8.11	12.1	0.103
PECS	2p	Total	12.7	23.4	36.1	0.136
CCC	2p	Total	12.9	23.9	36.7	0.134

collision were not available for comparison, and there are no known measurements of the differential cross sections of the metastable state.

Fully-differential ionization cross sections for e–H(2s) and e–H (2p) collisions at 14.8 eV are shown in figure 15 for several kinematic arrangements. The CCC H(2s) results are in good agreement with our calculations. The TDCS results of the H(1s) collision with the same total energy are included so as to highlight the significantly different structure in the angular distribution of the slow electron. This is clearly demonstrated in the $E_1 = 1$ and 3 eV plots at $\theta_2 = 15^\circ$, where the H(2s) target has three large peaks compared with a single dominant peak in the ground-state collision. The physical reason for this difference may be due to the different number of nodes in the wavefunction of hydrogen 1s and 2s targets. We believe that the large differential cross sections of the metastable 2s state in these regions should encourage future experimental confirmation of the TDCS structure revealed by our calculations.

6. Ionization threshold laws

The most computationally difficult energy region for PECS, and indeed most numerical methods, is near the ionization threshold where large grids are required to obtain converged

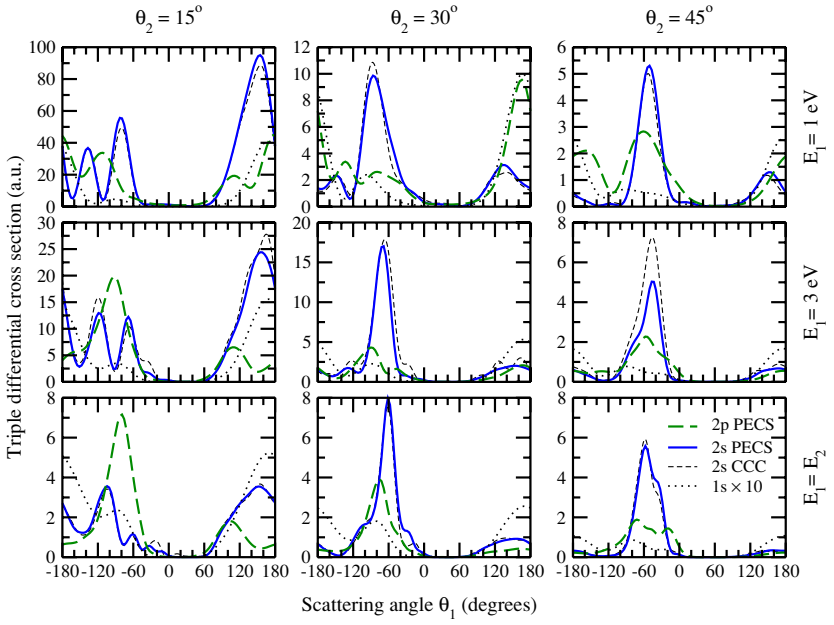

Figure 15. PECS coplanar TDCS results for e–H(2s) and e–H(2p) ionizing collisions at $E_0 = 14.8$ eV, compared with e–H(1s) at $E_0 = 25.0$ eV, for various fixed angles of the fast electron (θ_2) and energies of the slow electron (E_1). All collisions have the same total energy of $E = 11.4$ eV, and the e–H (1s) results have been multiplied by 10. 1s calculations include $L \leqslant 12$ and the 2s and 2p calculations include $L \leqslant 25$. CCC calculations from Bray [69].

ionization results and strong partial-wave coupling causes iterative solution methods to fail; both the iterative-coupling method of PECS and the CGS sparse-matrix solver used by ECS [23]. Fortunately, PECS can obtain solutions without iterative coupling, albeit with a higher computational overhead, so we were able to undertake a comprehensive investigation into the near-threshold region. Prior to this, no complete solution to the full Schrödinger equation had been undertaken with sufficient accuracy at energies approaching the ionization threshold to confirm the threshold laws predicted by classical, semiclassical and approximate quantal methods. We will first give a brief overview of the predictions made by these methods.

In 1953, Wannier [29] proposed an ionization threshold law for *all* ionizing collisions that lead to two free electrons leaving a charged atomic ion. This was achieved by dividing coordinate space into three regions, the reaction zone, Coulomb zone and free zone, and arguing that near threshold the probability of ionization is determined solely by the behaviour of the outgoing electrons in the Coulomb zone, where their motion can be described using classical mechanics. The reaction zone extends from the nucleus to approximately the Bohr radius, where quantum mechanics is required to describe the motion of the electrons. The outer boundary of the Coulomb zone is given as $\rho = (4Z - 1)/(\sqrt{2}E)$, which gives $\rho E \approx 2$ for $Z = 1$. In the free zone, Wannier postulated that the outgoing electrons essentially move independently of each other. As the reaction zone is inaccessible to classical mechanics, he also postulated that the distribution of the two electrons in phase space is approximately uniform when they exit the reaction zone.

Using these postulates, and considering the energy dependence of the classical trajectories in the Coulomb zone and an approximation of the Coulomb potential energy in this region,

Wannier calculated that the probability of a collision leading to ionization is $\sigma \propto E^{\eta}$ near ionization threshold. E is the total energy of the system and η is a constant that depends on the charge of the final-state ion and is given by

$$\eta = \frac{1}{4}\left[\left(\frac{100Z-9}{4Z-1}\right)^{1/2} - 1\right]. \tag{61}$$

For the electron-impact ionization of a hydrogen target this gives $\eta \approx 1.127$.

Wannier's threshold law applies to a vast range of atomic collisions, and consequently it continues to attract considerable interest five decades later. Experiments [77–81] have given support to this threshold law, and numerous semiclassical and quantal studies [82–89], which utilize approximations to the Schrödinger equation, are in agreement with Wannier's conjecture.

Wannier theory also predicts that the ionized and scattered electrons emerge in opposite directions ($\theta_{12} = \pi$) at threshold. As the total energy approaches threshold, θ_{12} is predicted to have a Gaussian probability distribution, centred at $\theta_{12} = \pi$, with a full-width-half-maximum (FWHM) related to total energy by $(\theta_{12})_{\mathrm{FWHM}} = \alpha E^{1/4}$ [90], where α is a constant of proportionality. Later investigations [87, 88, 91, 92] concur with this prediction though they give a range of values for α.

Semiclassical and quantal investigations have given important insights into near-threshold collisions, but have relied on one or more *a priori* assumptions to make the computations tractable: They (a) consider only collisions with zero total angular momentum ($L = 0$) and use semiclassical arguments [84, 85, 93] for similar scaling of partial waves with higher angular momentum, (b) use Wannier's conjecture that the interaction is limited to the Coulomb zone, (c) assume that the potential ridge at $\theta_{12} = \pi$ and $r_1 \approx r_2$ dominates the interaction, or (d) use a semiclassical approximation of the final-state wavefunction.

To date, several state-of-the-art fully-quantal numerical methods have been used to explore near-threshold e–H ionizing collisions. Kato and Watanabe [94] used their HSCC method to investigate the Wannier exponent in a two dimension model, angular correlation of the outgoing electrons for the $L = 0$ singlet partial wave and calculated the TICS and spin asymmetry of the full problem near threshold. Scott *et al* [95] used IERM to investigate the $L = 0$ singlet TICS near threshold. Yet, none of these methods have been implemented with the necessary precision to calculate η or the energy dependence of θ_{12} for the full e–H collision. The most comprehensive set of calculations thus far included those of Kato and Watanabe [96] and the PECS collinear model calculations completed during this project [34], both of which incorporated assumptions (a) and (c) and are consistent with the Wannier threshold law.

In this section, we will review our direct solutions of the *full* Schrödinger equation for near-threshold e–H ionizing collisions [39]. These *ab initio* fully-quantal PECS calculations were used to find the Wannier threshold law exponent η and investigate the behaviour of the spin asymmetry, SDCS (w.r.t. electron energy-sharing) and the energy dependence of θ_{12} near threshold.

6.1. Wannier threshold law

We performed calculations at 261 total energies between 0.01–0.10 au, spaced at 0.00025 au intervals below 0.05 au, and 0.0005 au above. The TICS were converged, w.r.t. grid spacing and angular momenta, to around $\pm 1\%$ over this energy range. For all the singlet calculations the PECS iterative-coupling method failed to converge and solutions were obtained using our fully-coupled method ($n_{\mathrm{g}} = 1$). However, the energy perturbation method did converge over a useful range of energies, allowing solutions to be obtained for $\Delta E \leqslant 0.0025$ au below

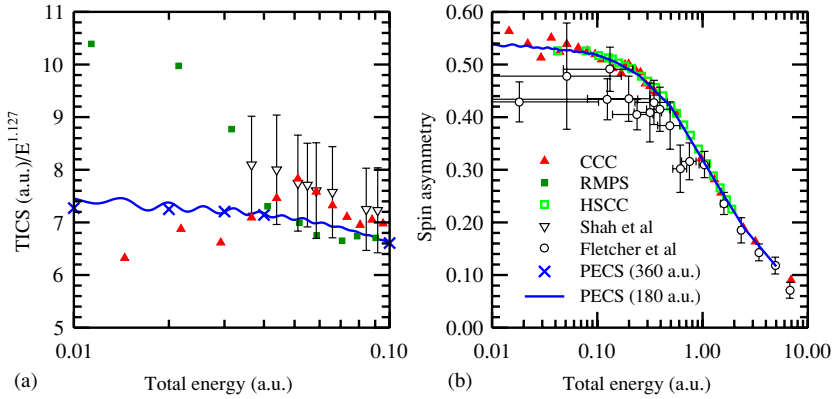

Figure 16. (a) PECS TICS for e–H collisions with $E = 0.01$–0.10 au ($R_0 = 180$ au and $R_0 = 360$ au) divided by $E^{1.127}$. (b) PECS spin asymmetry of e–H collisions for $E = 0.01$–5.0 au. Both plots share the same legend. HSCC [94], RMPS and CCC [15] calculations and measurements of Fletcher *et al* [97] and Shah *et al* [98] are also shown.

$E = 0.05$ au and $\Delta E \leqslant 0.0050$ au above $E = 0.05$ au. This provided a many-fold reduction in computational effort. All calculations used the same grid spacing and grid size ($R_0 = 180$ au), and included six partial waves ($L \leqslant 5$) to achieve the stated convergence at all energies. Angular momenta (l_1, l_2) were included for $n_L \leqslant 5$, 4, 3, 2, 2 and 1 for $L = 0$ through 5, respectively.

In figure 16(a), we plot our TICS results, which are divided by $E^{1.127}$ to emphasize the results at low energy. With this scaling we would expect the curves to become linear (ignoring E-dependent oscillations) if the Wannier threshold law is valid as threshold is approached. This is indeed the case and gives strong evidence that our TICS results are consistent with Wannier's threshold law. Though, the linear dependence upon energy implies that it only strictly applies at threshold. We have also included TICS results for several calculations undertaken with $R_0 = 360$ au, which are well within the estimated error of the $R_0 = 180$ au results. The scaling in this plot emphasizes the greatly reduced E-dependent oscillations of the PECS results compared with the RMPS and CCC calculations of Bartschat and Bray [15]. Overall, our estimated TICS error ranged between 1.5% at 0.10 au to 3% at 0.01 au. Our results match the ECS calculation [23] at 0.0735 au ($E_0 = 15.6$ eV, the only published ECS TICS result in this region), agree with [98] within experimental uncertainty, but are only in general agreement with CCC and RMPS calculations [15].

Semiclassical studies [84, 85, 93] predicted that the TICS contribution from each LS partial wave separately obeys the Wannier threshold law (with same η), with the exception of the $L = 0$ triplet partial wave for e–H collisions. This partial wave is highly suppressed due to the Pauli exclusion principle and was predicted [85, 93] to have $\eta \approx 3.88$, but later corrected by Peterkop [86] to $\eta \approx 3.38$. These predictions were also confirmed by our calculations.

In order to estimate the threshold power laws we performed nonlinear fitting of our results to the function $E^{\eta} \sum_{j=0}^{j_{\max}} c_j E^j$. This method was used previously by Kato and Watanabe [96] and also in our PECS collinear model investigation [34], and has the advantage that it allows for deviations from the power law away from threshold. The fitting function coefficients and their errors are sensitive to both $j_{\max}$ and the energy range chosen. We chose the largest $j_{\max}$ that minimized χ^2 without resulting in exponential increases in c_j or large errors in $c_{j_{\max}}$. Our calculations were fitted over several ranges of energies (0.01–0.03 au through 0.01–0.10 au, in

0.01 au increments), which gave the average and standard deviation of η as $\sigma \propto E^{1.122\pm0.015}$, and hence provides strong support for the Wannier threshold law. Nonlinear fitting of the $L = 0$ triplet partial cross section gave $\sigma \propto E^{3.36\pm0.02}$, in agreement with Peterkop [86].

Given the consistency of our results with the classical and semiclassical results, we can give the constants of proportionality and first-order energy-correction coefficients of these threshold laws for e–H collisions that best fit our results as

$$\sigma = E^{1.127}\{(7.49 \pm 0.03) - (8.7 \pm 1.1)E\} \tag{62}$$

$$\sigma_{L=0\,S=1} = E^{3.38}\{(1.199 \pm 0.005) - (6.0 \pm 0.2)E\}. \tag{63}$$

These functions give accurate σ for $E \leqslant 0.05$ au. The relatively large coefficient of the linear energy correction term gives important confirmation that the Wannier threshold law is strictly only valid at the ionization threshold.

6.2. Spin asymmetry

Spin asymmetry (A_s) is a purely quantum-mechanical concept and cannot be predicted using classical mechanics. Semiclassical analysis [93] suggests that A_s is independent of energy near threshold, using the argument that singlet and triplet channels have the same Wannier power-law exponent[2]. Though previous quantal calculations [15, 94] are consistent with this energy independence, their scatter or insufficient penetration into the threshold region leads to some uncertainty as to the value at threshold. We reproduce our results [39] along with experiment [97] and other calculations for A_s in figure 16(b). They confirm a linear, nearly energy-independent behaviour below 0.05 au and that the spin asymmetry approaches the limiting value $A_s = 0.54 \pm 0.01$. This is about 10% higher than experimental data but it should be noted that the error bars for $E \leqslant 0.3$ au are large.

6.3. Electron–electron angular distribution

The remaining important prediction of Wannier theory that we investigated was the angular dependence of the outgoing electrons.

As the total energy approaches ionization threshold, the size of the interaction region (Coulomb zone) increases approximately as $1/E$. This implies that ρE is a suitable radial measure when investigating the radial convergence of collisions with different total energies. In figure 17(a), we present $(\theta_{12})_{\mathrm{FWHM}}/E^{1/4}$ as a function of ρE at several total energies. For our results to support the $(\theta_{12})_{\mathrm{FWHM}} = \alpha E^{1/4}$ power law, then each curve within the threshold energy region should converge to the same constant α. Though we cannot demonstrate complete radial convergence at all energies due to our limited R_0, all the curves overlap and have the same convergence behaviour w.r.t. ρE, indicating that α converges to approximately 3.0 for $E \leqslant 0.05$ au. There is a slight deviation for the $E = 0.10$ au curve, but we consider that this is outside of the applicable energy range of the threshold law.

In order to demonstrate full convergence at 0.01 au, we estimate that our calculations need to be extended to at least $\rho E = 20$ ($\rho = 2000$ au at $E = 0.01$ au). As the computational effort of PECS scales as $O(N^4)$, where N is the number of grid points along one dimension, these calculations are well beyond the capacity of our present supercomputing facilities. However, further investigation of the convergence of our results that support these conclusions are given in [32] and we have estimated the threshold asymptotic value as $\alpha = 3.0 \pm 0.2$, in atomic

[2] This argument only holds for the summed partial waves as the $L = 0$ triplet partial-wave has a different η, but doesn't contribute to the sum as it is highly suppressed.

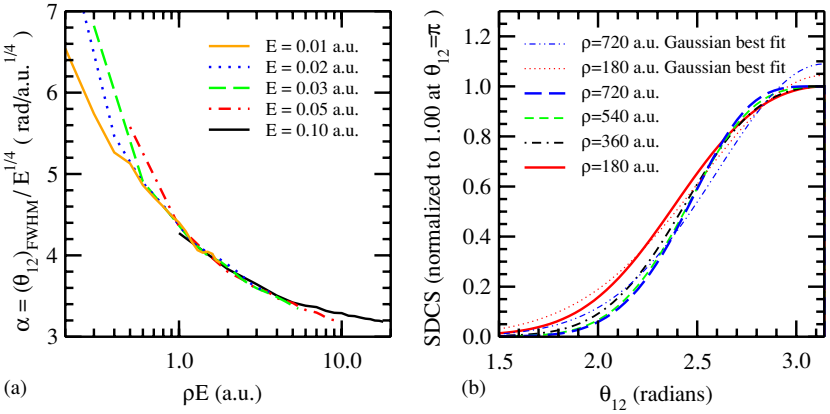

Figure 17. (a) Convergence of PECS $(\theta_{12})_{\mathrm{FWHM}}$ w.r.t. ρE, scaled by $E^{1/4}$, for e–H collisions at several near-threshold total energies. (b) PECS SDCS (w.r.t. θ_{12}) and Gaussian best-fit at $E = 0.01$ au for the $L = 0$ singlet partial-wave at various hyperradii.

units. Semiclassical calculations for α are reported as 2.66 [92], 2.71 [87], 3.38 [91] and 3.55 [88], and are markedly different from the experimental result of 1.6 ± 0.1 given by Cvejanović and Read [78]. Reasons for disagreement with experiment have been suggested as possible experimental error [88] and that the single plane of measurement (90° to the incident electron) is not representative of the full problem [92]. However, despite the variation of the constant of proportionality across the various models, our calculations support the $E^{1/4}$ energy dependence of the FWHM, and our calculation of α lies within the midrange of semiclassical calculations.

To evaluate α, most semiclassical calculations assumed a Gaussian shape for the θ_{12} SDCS (as in [83] but in disagreement with [88]) and all are limited to $L = 0$. Our SDCS results for the full e–H problem at $\rho E = 1.8$, near threshold, exhibit an approximate Gaussian shape but deviate systematically from this shape with increasing ρ. To investigate this further, figure 17(b) presents the normalized θ_{12} SDCS for the $L = 0$ singlet partial wave at various hyperradii from 180 au to 720 au. From this we see that as the hyperradius is increased the FWHM becomes narrower and the peak of the curve becomes flatter. For the 180 au and 720 au curves we also give the Gaussian curve that provides the best least-squares fit. It is clear that as the hyperradius increases the SDCS deviates further from the Gaussian approximation, and indeed the shape is closer to that predicted by Read [88] in the region $\theta_{12} > 2.5$ rad. Our results support a non-Gaussian form, which gives a further reason for the variance between our estimate for α and the semiclassical estimates.

Finally, to demonstrate the accuracy of our PECS method at very low energies, we reproduce our recent e–H DDCS and TDCS calculations from [42] in figure 18. These calculations were made in the perpendicular plane, and while cross sections in this plane are small, relative to coplanar geometries, they are known to provide a stringent test of theoretical models [99]. These PECS calculations are in excellent agreement with recent measurements, both in magnitude and shape, for projectile energies to within 0.5 eV of ionization threshold, including highly asymmetric energy sharing where the energy of the slow electron is as low as 0.05 eV. These are believed to be the first out-of-plane state-of-the-art calculations, and measurements, for e–H collisions. The evolution of the 'double collision' peak at $\theta_{12} = 104°$ is responsible for the deviation of the e–H cross sections from the $E^{1/4}$ power law at

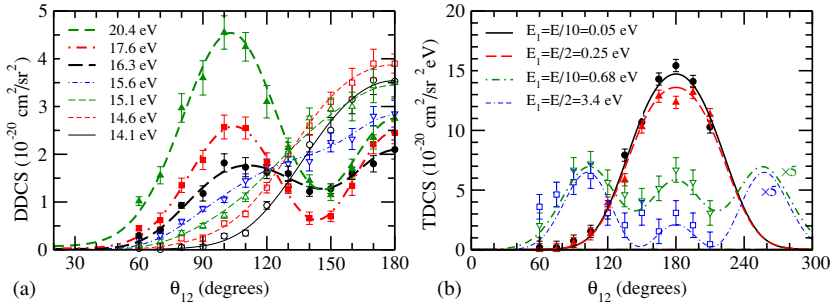

Figure 18. (a) PECS DDCS (w.r.t. θ_{12}) results in the perpendicular plane at various incident energies. (b) PECS TDCS results at various total energies and energy-sharing arrangements. Measurements are from Williams *et al* [42].

higher energies, and hence signals the breakdown of the Wannier threshold laws. An important conclusion drawn from these results was that this secondary peak evolves as a *linear* function of E and hence provided strong theoretical and experimental evidence that the Wannier threshold law is only strictly valid at the ionization threshold.

7. Conclusion

During this PhD project we undertook the theoretical and computational development of the PECS method, and presented a large set of calculations together with comparisons with other state-of-the-art computational methods and measurements. This has extended the ECS method [24] to include hydrogen and hydrogenic targets of arbitrary initial state and charge, and shown that the PECS method is capable of highly accurate calculations for a complete range of collisions, including elastic and inelastic collisions below and above ionization threshold, high-energy ionizing collisions and very low-energy ionizing collisions.

Several computational strategies were incorporated into the PECS method that proved to be highly efficient, including a propagation algorithm, iterative coupling and energy perturbation. These led to a dramatic improvement in its computational efficiency at higher energies, and significantly reduced the computational effort at closely spaced energies.

All the PECS calculations presented in this tutorial, and other publications emanating from this research [33–43], are in excellent agreement with other state-of-the-art computational methods and measurements, where available. We consider that the PECS method now offers *complete* solutions for e–H collisions in four important respects.

- Solutions are obtained by a direct solution of the full Schrödinger equation and all errors due to numerical discretization and finite grid size are *demonstrated* to converge consistently with grid-spacing reduction, hyperradius extension and increased number of partial waves.
- Results can be obtained at all energies accessible to experiment, within the constraints of the non-relativistic Schrödinger equation, up to high energies where perturbation methods become accurate.
- Gives benchmark solutions over the whole range of observables accessible to experiment, for both discrete final-state and ionizing collisions.
- Solves electron collisions with hydrogenic ions of arbitrary nuclear charge and initial state.

This is significant in that it is the first method to demonstrate benchmark *ab initio* results over a complete range of hydrogenic targets, impact energies and final-state kinematic arrangements.

The ECS method has recently been applied to other three-body problems including photon–helium collisions [100] and photoionization of hydrogen molecules [101]. Yet, there remain many other three-body systems to which the PECS method can be applied, of which the positron–hydrogen collision system is a prime candidate.

The full solution to the Schrödinger equation for a four-body break-up collision is much more computationally demanding than the three-body collisions investigated here, and is presently under investigation with the PECS method. The ECS method has very recently been applied to electron–helium collisions in the s-wave model using a *time-dependent* ECS method [102], and we expect that the PECS method will make similar progress with the time-independent solutions. Ultimately, a full four-body solution to electron–helium collisions will give accurate information on many processes that are largely inaccessible to existing three-body approaches, including double excitation, excitation–ionization and double ionization.

Certainly each new collision system will present its own difficulties and challenges, but we believe that the developments summarized in this tutorial will significantly aid these future efforts.

Acknowledgments

I would like to thank Professor Andris Stelbovics, my principal PhD supervisor, for his tremendous support and good counsel. His encouragement and enthusiasm for this project was unwavering. I am also indebted to Professor Igor Bray, my co-supervisor, whom offered much valuable advice and performed many CCC calculations for inclusion in this tutorial. I also acknowledge the support of the Western Australian Interactive Virtual Environments Centre and the Australian Partnership for Advanced Computing for providing supercomputing facilities to support this research.

Appendix A. Reduced matrix element of $\frac{1}{r_{12}}$

The matrix element of $\frac{1}{r_{12}}$ used in (16) is given by

$$\langle l_1' l_2' L' M' | \frac{1}{r_{12}} | l_1 l_2 L M \rangle = \sum_{\lambda} \frac{r_>^{\lambda}}{r_>^{\lambda+1}} f_\lambda(l_1, l_2, l_1', l_2'; L) \delta_{LL'} \delta_{MM'}, \tag{A.1}$$

where

$$f_\lambda(l_1, l_2, l_1', l_2'; L) = (-1)^{L+l_2+l_2'} [l_1][l_2][l_1'][l_2'] \begin{Bmatrix} l_1 & l_2 & L \\ l_2' & l_1' & \lambda \end{Bmatrix} \begin{pmatrix} l_1 & \lambda & l_1' \\ 0 & 0 & 0 \end{pmatrix} \begin{pmatrix} l_2 & \lambda & l_2' \\ 0 & 0 & 0 \end{pmatrix}, \tag{A.2}$$

$[l] = \sqrt{2l+1}$, and where the λ summation is over all non-negative integers such that the Wigner-3j (round brackets) and Wigner-6j (braces) symbols are nonzero. This occurs when

$$\max(|l_1 - l_1'|, |l_2 - l_2'|) \leqslant \lambda \leqslant \min(|l_1 + l_1'|, |l_2 + l_2'|). \tag{A.3}$$

An important outcome of this matrix element is that it is nonzero only when $L = L'$ and $M = M'$, and has no dependence upon the projection of the angular momenta M, m_1 or m_2. We refer to it as the reduced matrix element of $\frac{1}{r_{12}}$, which is represented by

$$\langle l_1' l_2' \| \frac{1}{r_{12}} \| l_1 l_2 \rangle_L \equiv \langle l_1' l_2' L' M' | \frac{1}{r_{12}} | l_1 l_2 L M \rangle \delta_{LL'} \delta_{MM'}, \tag{A.4}$$

and note from the Wigner-6j and Wigner-3j symmetry properties that

$$\langle l_1' l_2' \| \frac{1}{r_{12}} \| l_1 l_2 \rangle_L = \langle l_2' l_1' \| \frac{1}{r_{12}} \| l_2 l_1 \rangle_L = \langle l_1 l_2 \| \frac{1}{r_{12}} \| l_1' l_2' \rangle_L. \tag{A.5}$$

Appendix B. Numerov formulae

In section 3.2, we derived a one-dimensional variable-grid Numerov formula for solving second-order differential equations. However, it was necessary to derive nine variations of this Numerov formula in order to compute the e–H scattering wavefunction on a two-dimensional grid. The formula selection depends on whether $r_{i-1} = 0$ and/or $r_{j-1} = 0$, dictating whether a series expansion for ψ_{ij} is used when deriving the formula, and when this expansion is used, whether the angular momentum of the electron l is zero or greater than zero. These Numerov formulae are used to solve equations of the form

$$\left(\frac{\partial^2}{\partial r_i^2} + \frac{\partial^2}{\partial r_j^2} \right) \overline{\psi}^{LMS\Pi}_{i,l_1 l_2}(r_i, r_j) + \overline{\Omega}^{LMS\Pi}_{i,l_1 l_2}(r_i, r_j) = 0, \tag{B.1}$$

and may be most simply presented as

$$\sum_{i'=-1}^{1} \sum_{j'=-1}^{1} \left\{ \left(h^2 \mathcal{B}_{i'} \mathcal{C}_{j'} + t^2 \mathcal{A}_{i'} \mathcal{D}_{j'} \right) \overline{\psi}^{LMS\Pi}_{i,l_1 l_2}(r_{i+i'}, r_{j+j'}) + h^2 t^2 \mathcal{B}_{i'} \mathcal{D}_{j'} \overline{\Omega}^{LMS\Pi}_{i,l_1 l_2}(r_{i+i'}, r_{j+j'}) \right\} = 0, \tag{B.2}$$

where $\overline{\Omega}^{LMS\Pi}_{i,l_1 l_2}$ can be evaluated from (16) and (17), giving

$$\begin{aligned} \overline{\Omega}^{LMS\Pi}_{i,l_1 l_2}(r_i, r_j) = & \left\{ 2E + 2Z \left(\frac{1 - \delta_{i,0}}{r_i} + \frac{1 - \delta_{j,0}}{r_j} \right) - \frac{l_1(l_1+1)(1-\delta_{i,0})}{r_i^2} \right. \\ & \left. - \frac{l_2(l_2+1)(1-\delta_{j,0})}{r_j^2} \right\} \overline{\psi}^{LMS\Pi}_{i,l_1 l_2}(r_i, r_j) - 2\overline{\chi}^{LMS\Pi}_{i,l_1 l_2}(r_i, r_j) \\ & - 2 \sum_{l_1' l_2'} \langle l_1 l_2 \| \frac{1}{r_{12}} \| l_1' l_2' \rangle_L \, \overline{\psi}^{LMS\Pi}_{i,l_1' l_2'}(r_i, r_j). \end{aligned} \tag{B.3}$$

Note that the $\boldsymbol{i}$ subscript on the $\overline{\psi}$ and $\overline{\chi}$ functions uses bold font to differentiate this abbreviation for the initial state from the grid points in the i direction. Also, note that the singularities in $\overline{\Omega}^{LMS\Pi}_{i,l_1 l_2}$ are removed by the use of delta functions.

The grid spacing is given by $h = r_i - r_{i-1}$ and $t = r_j - r_{j-1}$ in the i and j directions, respectively. Two further coefficients are used, $\alpha = (r_{i+1} - r_i)/h$ and $\beta = (r_{j+1} - r_j)/t$, which determine the expansion (or contraction) of the grid spacing in the i and j directions, respectively. Each grid measurement, h, t, α and β may be real or complex, and are displayed graphically in figure 2. The values of $\mathcal{A}$, $\mathcal{B}$, $\mathcal{C}$ and $\mathcal{D}$ vary depending on whether $r_{i-1} = 0$ and/or $r_{j-1} = 0$ and the angular momentum of the electrons.

Firstly, we shall consider only the i direction. If there is no singularity, $r_{i-1} > 0$, then

$$\begin{aligned} \mathcal{A}_{-1} &= 12\alpha \\ \mathcal{A}_0 &= -12(\alpha + 1) \\ \mathcal{A}_1 &= 12 \\ \mathcal{B}_{-1} &= -\alpha^3 + \alpha^2 + \alpha \\ \mathcal{B}_0 &= \alpha^3 + 4\alpha^2 + 4\alpha + 1 \\ \mathcal{B}_1 &= \alpha^2 + \alpha - 1. \end{aligned} \tag{B.4}$$

If there is a singularity ($r_{i-1} = 0$) and $l = 0$ then

$$\begin{aligned}
\mathcal{A}_{-1} &= 0 \\
\mathcal{A}_0 &= (\alpha+1)\left(3\lambda_1^2\alpha^2h^2 + 4\lambda_1^2h^2\alpha - 30\lambda_1\alpha h + \lambda_1^2h^2 - 24\lambda_1 h + 72\right) \\
\mathcal{A}_1 &= -\lambda_1^2h^2 - 6\lambda_1\alpha h + 2\lambda_1^2h^2\alpha + 24\lambda_1 h - 72 \\
\mathcal{B}_{-1} &= 6\alpha(\alpha^2 - \alpha - 1) \\
\mathcal{B}_0 &= (\alpha+1)(3\lambda_1\alpha^2h - 6\alpha^2 - 18\alpha + 4\lambda_1\alpha h + \lambda_1 h - 6) \\
\mathcal{B}_1 &= 2\lambda_1\alpha^2h - 6\alpha^2 + \lambda_1\alpha h - \lambda_1 h - 6\alpha + 6,
\end{aligned} \tag{B.5}$$

or if there is a singularity and $l > 0$ then

$$\begin{aligned}
\mathcal{A}_{-1} &= 0 \\
\mathcal{A}_0 &= (1+\alpha)^{2+l}(\alpha(2+l)(l^2 + l + \lambda_2 + \lambda_1 h) - 6 - 9l + \lambda_2 - 3l^2 + \lambda_1 h) \\
\mathcal{A}_1 &= \alpha^2\lambda_1 h(l+1) + \alpha(l^3 + 6l^2 + (\lambda_1 h + \lambda_2 + 11)l + \lambda_2 + 6) + 9l + 6 - \lambda_1 h - \lambda_2 + 3l^2 \\
\mathcal{B}_{-1} &= 0 \\
\mathcal{B}_0 &= (1+\alpha)^{2+l}(l\alpha + 2\alpha + 1) \\
\mathcal{B}_1 &= (1+\alpha)^2(l\alpha + \alpha - 1).
\end{aligned} \tag{B.6}$$

In these equations $\lambda_1 = 2Z$, where Z is the charge on the nucleus, and $\lambda_2 = -l(l+1)$, where l is the angular momentum of the electron (l_1 and l_2 for the i and j directions, respectively).

For the j direction, the formulae are based on those given above and are selected depending on whether there is a singularity ($r_{j-1} = 0$) and the angular momentum of the electron $l = l_2$. For the j direction we use $\mathcal{C}$ in place of $\mathcal{A}$ and $\mathcal{D}$ in place of $\mathcal{B}$, and replace α with β and h with t. We now have the required values for $\mathcal{A}$, $\mathcal{B}$, $\mathcal{C}$ and $\mathcal{D}$ that are used in (B.2) to give the Numerov formula relationship between the nine grid points centred on (i, j).

References

[1] Massey H S W and Mohr C B O 1932 *Proc. R. Soc.* A **136** 289
[2] Massey H S W and Mohr C B O 1934 *Proc. R. Soc.* A **146** 880
[3] Mott N F and Massey H S W 1949 *Theory of Atomic Collisions* 2nd edn (Oxford: Clarendon)
[4] Omidvar K 1965 *Phys. Rev.* **140** A26
[5] Burke P G and Taylor A J 1966 *Proc. Phys. Soc.* **88** 549
[6] Burke P G and Webb T G 1970 *J. Phys. B: At. Mol. Phys.* **3** L131
[7] Bray I and Stelbovics A T 1992 *Phys. Rev. Lett.* **69** 53
[8] Bray I and Stelbovics A T 1995 *Comput. Phys. Commun.* **85** 1
[9] Bray I and Stelbovics A T 1992 *Phys. Rev.* A **46** 6995
[10] Bray I and Stelbovics A T 1995 *Adv. At. Mol. Phys.* **35** 209
[11] Burke P G, Noble C J and Scott M P 1987 *Proc. R. Soc.* A **410** 289
[12] Scott M P, Scholz T T, Walters H R J and Burke P G 1989 *J. Phys. B: At. Mol. Opt. Phys.* **22** 3055
[13] Scholz T T, Walters H R J, Scott M P and Burke P G 1991 *J. Phys. B: At. Mol. Opt. Phys.* **24** 2097
[14] Bray I and Stelbovics A T 1993 *Phys. Rev. Lett.* **70** 746
[15] Bartschat K and Bray I 1996 *J. Phys. B: At. Mol. Opt. Phys.* **29** L577
[16] Kato D and Watanabe S 1995 *Phys. Rev. Lett.* **74** 2443
[17] Colgan J, Pindzola M S, Robicheaux F J, Griffin D C and Baertschy M 2002 *Phys. Rev.* A **65** 042721
[18] Bray I 2000 *Aust. J. Phys.* **53** 355
[19] Scott M P, Stitt T, Scott N S and Burke P G 2002 *J. Phys. B: At. Mol. Opt. Phys.* **35** L323
[20] Bray I 1997 *Phys. Rev. Lett.* **78** 4721
[21] Stelbovics A T 1999 *Phys. Rev. Lett.* **83** 1570
[22] Rescigno T N, Baertschy M, Isaacs W A and McCurdy C W 1999 *Science* **286** 2474
[23] Baertschy M, Rescigno T N and McCurdy C W 2001 *Phys. Rev.* A **64** 022709
[24] McCurdy C W, Baertschy M and Rescigno T N 2004 *J. Phys. B: At. Mol. Opt. Phys.* **37** R137
[25] Nicolaides C A and Beck D R 1978 *Phys. Lett.* A **65** 11
[26] Simon B 1979 *Phys. Lett.* A **71** 211

[27] Peterkop R K 1977 *Theory of Ionization of Atoms by Electron Impact* (Boulder, CO: Colorado Associated University Press)
[28] McCurdy C W, Horner D A and Rescigno T N 2001 *Phys. Rev.* A **63** 022711
[29] Wannier G H 1953 *Phys. Rev.* **90** 817
[30] Poet R 1980 *J. Phys. B: At. Mol. Phys.* **13** 2995
[31] Jones S and Stelbovics A T 2000 *Phys. Rev. Lett.* **84** 1878
[32] Bartlett P L 2005 *PhD Thesis* Murdoch University, Perth, Australia, http://adt.caul.edu.au
[33] Bartlett P L, Bray I, Jones S, Stelbovics A T, Kadyrov A S, Bartschat K, Ver Steeg G L, Scott M P and Burke P G 2003 *Phys. Rev.* A **68** 020702(R)
[34] Bartlett P L, Stelbovics A T and Bray I 2003 *Phys. Rev.* A **68** 030701(R)
[35] Bartlett P L and Stelbovics A T 2004 *Phys. Rev.* A **69** 022703
[36] Bartlett P L, Stelbovics A T and Bray I 2004 *J. Phys. B: At. Mol. Opt. Phys.* **37** L69
[37] Stelbovics A T, Bartlett P L, Bray I and Kadyrov A S 2004 *Phys. Scr.* T **110** 247
[38] Bartlett P L and Stelbovics A T 2004 *Phys. Rev.* A **69** 040701(R)
[39] Bartlett P L and Stelbovics A T 2004 *Phys. Rev. Lett.* **93** 233201
[40] Bartlett P L, Stelbovics A T, Lee G M and Bray I 2005 *J. Phys. B: At. Mol. Opt. Phys.* **38** L95
[41] Williams J F, Bartlett P L, Bray I, Stelbovics A T and Mikosza A G 2006 *J. Phys. B: At. Mol. Opt. Phys.* **39** 719
[42] Williams J F, Bartlett P L and Stelbovics A T 2006 *Phys. Rev. Lett.* **96** 123201
[43] Bartlett P L, Williams J F, Bray I, Mikosza A G and Stelbovics A T 2006 *Phys. Rev.* A **74** 022714
[44] Rescigno T N, Baertschy M, Byrum D and McCurdy C W 1997 *Phys. Rev.* A **55** 4253
[45] McCurdy C W, Rescigno T N and Byrum D 1997 *Phys. Rev.* A **56** 1958
[46] Brink D M and Satchler G R 1993 *Angular Momentum* 3rd edn (New York: Oxford University Press)
[47] Varshalovich D A, Moskalev A N and Khersonskii V K 1988 *Quantum Theory of Angular Momentum* (Singapore: World Scientific)
[48] Baertschy M, Rescigno T N, Isaacs W A, X. Li and McCurdy C W 2001 *Phys. Rev.* A **63** 022712
[49] McCurdy C W, Horner D A and Rescigno T N 2002 *Phys. Rev.* A **65** 042714
[50] Kadyrov A S, Mukhamedzhanov A M and Stelbovics A T 2003 *Phys. Rev.* A **67** 024702
[51] Kadyrov A S, Mukhamedzhanov A M, Stelbovics A T and Bray I 2004 *Phys. Rev.* A **70** 062703
[52] Jones S and Stelbovics A T 1999 *Aust. J. Phys.* **52** 621
[53] Wang Y D and Callaway J 1993 *Phys. Rev.* A **48** 2058
[54] Wang Y D and Callaway J 1994 *Phys. Rev.* A **50** 2327
[55] Jones S and Stelbovics A T 2002 *Phys. Rev.* A **66** 032717
[56] Abramowitz M and Stegun I A 1965 *Handbook of Mathematical Functions with Formulas, Graphs and Mathematical Tables* (New York: Dover)
[57] Allison A C 1970 *J. Comput. Phys.* **6** 378
[58] Baertschy M, Rescigno T N, McCurdy C W, Colgan J and Pindzola M S 2001 *Phys. Rev.* A **63** 050701
[59] Childers J G, James K E, Bray I, Baertschy M and Khakoo M A 2004 *Phys. Rev.* A **69** 022709
[60] Temkin A 1962 *Phys. Rev.* **126** 130
[61] Poet R 1978 *J. Phys. B: At. Mol. Phys.* **11** 3081
[62] Peterkop R and Rabik L 1972 *J. Phys. B: At. Mol. Phys.* **5** 1823
[63] Temkin A and Hahn Y 1974 *Phys. Rev.* A **9** 708
[64] Gradziel M L and O'Neill R W 2004 *J. Phys. B: At. Mol. Opt. Phys.* **37** 1893
[65] Yalim H A, Cvejanović D and Crowe A 1999 *J. Phys. B: At. Mol. Opt. Phys.* **32** 3437
[66] Williams J F and Mikosza A G 2006 *J. Phys. B: At. Mol. Opt. Phys.* **39** 4113
[67] Bartschat K, Bray I, Burke P G and Scott M P 1996 *J. Phys. B: At. Mol. Opt. Phys.* **29** 5493
[68] Williams J F 1988 *J. Phys. B: At. Mol. Opt. Phys.* **21** 2107
[69] Bray I 2004 Private communication
[70] Bray I 2003 *J. Phys. B: At. Mol. Opt. Phys.* **36** 2203
[71] Ehrhardt H, Jung K, Knoth G and Schlemmer P 1986 *Z. Phys.* D **1** 3
[72] Thomson J J 1912 *Phil. Mag.* **23** 449
[73] Burgess A, Hummer D G and Tully J A 1970 *Phil. Trans. R. Soc.* A **266** 225
[74] Stia C R, Fojón O A and Rivarola R D 2000 *J. Phys. B: At. Mol. Opt. Phys.* **33** 1211
[75] Tinschert K, Muller A, Hofmann G, Huber K, Becker R, Gregory D C and Salzborn E 1989 *J. Phys. B: At. Mol. Opt. Phys.* **22** 531
[76] Defrance P, Claeys W, Cornet A and Poulaert G 1981 *J. Phys. B: At. Mol. Phys.* **14** 111
[77] McGowan J W and Clarke E M 1968 *Phys. Rev.* **167** 43
[78] Cvejanović S and Read F H 1974 *J. Phys. B: At. Mol. Phys.* **7** 1841
[79] Spence D 1975 *Phys. Rev.* A **11** 1539

[80] Pichou F, Huetz A, Joyez G and Landau M 1978 *J. Phys. B: At. Mol. Phys.* **11** 3683
[81] Donahue J B, Gram P A M, Hynes M V, Hamm R W, Frost C A, Bryant H C, Butterfield K B, Clark D A and Smith W W 1982 *Phys. Rev. Lett.* **48** 1538
[82] Peterkop R 1971 *J. Phys. B: At. Mol. Phys.* **4** 513
[83] Rau A R P 1971 *Phys. Rev.* A **4** 207
[84] Roth T A 1972 *Phys. Rev.* A **5** 476
[85] Klar H and Schlecht W 1976 *J. Phys. B: At. Mol. Phys.* **9** 1699
[86] Peterkop R 1983 *J. Phys. B: At. Mol. Phys.* **16** L587
[87] Feagin J M 1984 *J. Phys. B: At. Mol. Phys.* **17** 2433
[88] Read F H 1984 *J. Phys. B: At. Mol. Phys.* **17** 3965
[89] Rost J-M 1994 *Phys. Rev. Lett.* **72** 1998
[90] Vinkalns I and Gailitis M 1967 *Abstr. 5th Int. Conf. on the Physics of Electronic and Atomic Collisions* (Leningrad: Nauka) pp 648–50
[91] Rau A R P 1976 *J. Phys. B: At. Mol. Phys.* **9** L283
[92] Altick P L 1985 *J. Phys. B: At. Mol. Phys.* **18** 1841
[93] Greene C H and Rau A R P 1982 *Phys. Rev. Lett.* **48** 533
[94] Kato D and Watanabe S 1997 *Phys. Rev.* A **56** 3687
[95] Scott M P, Burke P G, Bartschat K and Bray I 1997 *J. Phys. B: At. Mol. Opt. Phys.* **30** L309
[96] Kato D and Watanabe S 1996 *J. Phys. B: At. Mol. Opt. Phys.* **29** L779
[97] Fletcher G D, Alguard M J, Gay T J, Hughes V W, Wainwright P F, Lubell M S and Raith W 1985 *Phys. Rev.* A **31** 2854
[98] Shah M B, Elliott D S and Gilbody H B 1987 *J. Phys. B: At. Mol. Phys.* **20** 3501
[99] Murray A J, Woolf M B J and Read F H 1992 *J. Phys. B: At. Mol. Opt. Phys.* **25** 3021
[100] Horner D A, Colgan J, Martín, McCurdy C W, Pindzola M S and Rescigno T N 2004 *Phys. Rev.* A **70** 064701
[101] Vanroose W, Martín F, Rescigno T N and McCurdy C W 2004 *Phys. Rev.* A **70** 050703(R)
[102] Horner D A, McCurdy C W and Rescigno T N 2005 *Phys. Rev.* A **71** 012701